Journal of Computational Physics 469 (2022) 111508

Contents lists available at ScienceDirect

Journal of Computational Physics

www.elsevier.com/locate/jcp

Fifth-order A-WENO schemes based on the path-conservative central-upwind method

Shaoshuai Chu [a], Alexander Kurganov [b], Mingye Na [a,*]

[a] Department of Mathematics, Southern University of Science and Technology, Shenzhen, 518055, China
[b] Department of Mathematics, SUSTech International Center for Mathematics and Guangdong Provincial Key Laboratory of Computational Science and Material Design, Southern University of Science and Technology, Shenzhen, 518055, China

ARTICLE INFO

Article history:
Received 31 July 2021
Received in revised form 9 June 2022
Accepted 22 July 2022
Available online 2 August 2022

Keywords:
A-WENO schemes
Semi-discrete central-upwind schemes
Path-conservative central-upwind schemes
Two-layer shallow water equations
Well-balanced schemes

ABSTRACT

We develop fifth-order A-WENO finite-difference schemes based on the path-conservative central-upwind method for nonconservative one- and two-dimensional hyperbolic systems of nonlinear PDEs. The main challenges in development of accurate and robust numerical methods for the studied systems come from the presence of nonconservative products. Semi-discrete second-order finite-volume path-conservative central-upwind (PCCU) schemes recently proposed in Castro Díaz et al. (2019) [8] provide one with a reliable Riemann-problem-solver-free numerical method for nonconservative hyperbolic system. In this paper, we extend the PCCU schemes to the fifth-order of accuracy in the framework of A-WENO finite-difference schemes.

We apply the developed schemes to the two-layer shallow water equations. We ensure that the developed schemes are well-balanced in the sense that they are capable of exactly preserving "lake-at-rest" steady states. We illustrate the performance of the new fifth-order schemes on a number of one- and two-dimensional examples, where one can clearly see that the proposed fifth-order schemes clearly outperform their second-order counterparts.

1. Introduction

This paper is focused on development of fifth-order A-WENO schemes based on the path-conservative central-upwind (PCCU) method. The schemes are designed for solving nonconservative one-dimensional (1-D) and two-dimensional (2-D) hyperbolic systems of nonlinear PDEs. A general form of the 1-D nonconservative system is

$$\boldsymbol{U}_t + \boldsymbol{F}(\boldsymbol{U})_x = B(\boldsymbol{U})\boldsymbol{U}_x, \tag{1.1}$$

where x is a spatial variable, t is the time, $\boldsymbol{U} \in \mathbb{R}^N$ is a vector of unknown variables, $\boldsymbol{F} : \mathbb{R}^N \to \mathbb{R}^N$ are nonlinear fluxes, and $B(\boldsymbol{U}) = (b_{m\ell}(\boldsymbol{U}))_{m,\ell=1}^N \in \mathbb{R}^{N\times N}$.

The nonconservative systems (1.1) arise in a number of fluid models within different contexts, such as the Saint-Venant system, multilayer shallow water equations, multiphase flow models, multicomponent fluid models, and many others.

Most of existing schemes for the system (1.1) are generalized from finite-volume (FV) schemes for nonlinear hyperbolic systems of conservation laws, which has the form

* Corresponding author.
E-mail addresses: 11930702@mail.sustech.edu.cn (S. Chu), alexander@sustech.edu.cn (A. Kurganov), 12131231@mail.sustech.edu.cn (M. Na).

https://doi.org/10.1016/j.jcp.2022.111508
0021-9991/

$$\boldsymbol{U}_t + \boldsymbol{F}(\boldsymbol{U})_x = \boldsymbol{0}. \tag{1.2}$$

Similar to the solutions of the system (1.2), the solutions of (1.1) can develop shocks, rarefactions, and contact discontinuities even when the initial data are smooth. Apart from this, the challenges for studying the system (1.1) theoretically and numerically mainly come from the presence of the nonconservative products on the right-hand side (RHS) when $B \neq 0$. In general, when $\boldsymbol{U}$ are discontinuous, weak solution of the system (1.1) can not be understood in the sense of distributions. Instead, one can introduce the weak solution of this system as the Borel measures as it was done in [15,29,30]. This concept of weak solutions was utilized to develop path conservative FV upwind schemes; see, e.g., the review papers [5,10,11,14,37,39,41] and reference therein.

In this paper, we focus on Riemann-problem-solver-free central-upwind (CU) schemes, which were originally introduced in [24,25,27,28] as a "black-box" solver for general multidimensional hyperbolic systems of conservation laws. In [8], the CU schemes were first reformulated into the path-conservative framework and then extended to the 1-D nonconservative systems (1.1). The resulting PCCU schemes provide one with a robust and quite accurate tool for solving nonconservative hyperbolic systems. However, the PCCU schemes from [8] are only second-order accurate, which limits their accuracy, and the resolution of certain practically important solutions (like the one containing internal waves in the two-layer shallow water systems) may not be sufficiently high unless a very fine mesh is used. In order to enhance the performance of the PCCU schemes, we extend them to the fifth order of accuracy via the alternative weighted essentially non-oscillatory (A-WENO) framework.

One of the popular classes of higher-order FV schemes is weighted essentially non-oscillatory (WENO) schemes, which employ special high-order WENO reconstructions to increase the spatial order (of accuracy) of the underlying FV schemes; see the review papers [42,43] and references therein. These reconstructions are quite complicated and computationally expensive, especially in the multidimensional case. Finite-difference (FD) WENO framework provides one with a less complicated way to develop higher-order WENO schemes as its reconstruction process is performed in a "dimension-by-dimension" manner. The original FD WENO schemes, proposed in [19], rely on a flux splitting, which is quite diffusive and thus affects the resolution of nonsmooth parts of the computed solutions, whereas the A-WENO schemes employ standard FV numerical fluxes without using any flux splitting. The A-WENO schemes were developed in [20] (see also [32,33,46,48]) for conservative systems (1.2). In [47], A-WENO schemes based on the CU fluxes have been introduced.

In this paper, we extend the second-order PCCU schemes to the fifth order of accuracy in both 1-D and 2-D using the A-WENO framework. The details on the proposed extension can be found in §4. As in [16,20,32,36,48], in order to reduce the magnitude of oscillations, we use the local characteristic decomposition in the WENO-Z interpolation employed to evaluate the FV fluxes.

The designed A-WENO PCCU schemes are applied to particular nonconservative systems—the 1-D and 2-D two-layer shallow water equations. These systems can be derived from the compressible isotropic Euler equations and have been widely used to study water flows in rivers, coastal areas, oceanography, and atmospheric sciences; see, e.g., [21,38,45,49]. For several existing numerical methods for two-layer shallow water equations, we refer the reader to, e.g., [1,2,4,8,13,22, 26,34,41] and references therein. Computing highly accurate solution of these models is a quite challenging task not only because the two-layer shallow water system is nonconservative, but also since internal waves typically contain intermediate states, which are quite hard to capture numerically when a coarse mesh is used. The Riemann-problem-solver-free second-order PCCU scheme provides one with a robust computational tool for the two-layer shallow water equations, which is, however, not sufficiently accurate and might require substantial mesh refinement to capture those intermediate states. The new fifth-order A-WENO PCCU scheme offers a simple, robust and still Riemann-problem-solver-free numerical tool for the two-layer shallow water equations. Indeed, we test both 1-D and 2-D fifth-order A-WENO PCCU schemes on several numerical examples and demonstrate their higher resolution compared with the original second-order PCCU schemes.

The rest of the paper is organized as follows. In §2, we briefly describe the 1-D second-order FV PCCU scheme. In §3, we provide a brief overview of the 1-D fifth-order A-WENO schemes for hyperbolic systems of conservation laws. In §4, we construct a new 1-D fifth-order A-WENO PCCU scheme. In §5, we extend the 1-D fifth-order A-WENO PCCU scheme to the 2-D nonconservative systems. In §6, we apply the developed fifth-order A-WENO PCCU schemes to the 1-D and 2-D two-layer shallow water equations. Finally, in §7, we present both the 1-D and 2-D numerical results.

2. 1-D second-order FV PCCU schemes: a brief overview

We first consider the nonconservative hyperbolic system (1.1) and briefly review the second-order FV PCCU scheme from [8].

We assume that the computational domain is covered with the uniform cells $C_j := [x_{j-\frac{1}{2}}, x_{j+\frac{1}{2}}]$ of size Δx centered at $x_j = (x_{j-\frac{1}{2}} + x_{j+\frac{1}{2}})/2$. We denote by $\overline{\boldsymbol{U}}_j(t)$ the cell average of $\boldsymbol{U}(\cdot,t)$ over the corresponding intervals C_j, namely

$$\overline{\boldsymbol{U}}_j(t) :\approx \frac{1}{\Delta x}\int\limits_{C_j} \boldsymbol{U}(x,t)\,\mathrm{d}x,$$

and suppose that at certain time $t \geq 0$, the cell average values $\overline{\boldsymbol{U}}_j$ are available. From here on, we suppress the time-dependence of all of the indexed quantities for the sake of brevity.

According to the PCCU scheme introduced in [8], the solution is then evolved in time by solving the following system of ODEs:

$$\frac{\mathrm{d}\overline{\boldsymbol{U}}_j}{\mathrm{d}t}=-\frac{1}{\Delta x}\left[\boldsymbol{H}_{j+\frac12}-\boldsymbol{H}_{j-\frac12}-\boldsymbol{B}_j-\frac{a^+_{j-\frac12}}{a^+_{j-\frac12}-a^-_{j-\frac12}}\boldsymbol{B}_{\boldsymbol{\Psi},j-\frac12}+\frac{a^-_{j+\frac12}}{a^+_{j+\frac12}-a^-_{j+\frac12}}\boldsymbol{B}_{\boldsymbol{\Psi},j+\frac12}\right], \tag{2.1}$$

where

$$\boldsymbol{H}_{j+\frac12}=\frac{a^+_{j+\frac12}\boldsymbol{F}(\boldsymbol{U}^-_{j+\frac12})-a^-_{j+\frac12}\boldsymbol{F}(\boldsymbol{U}^+_{j+\frac12})}{a^+_{j+\frac12}-a^-_{j+\frac12}}+\frac{a^+_{j+\frac12}a^-_{j+\frac12}}{a^+_{j+\frac12}-a^-_{j+\frac12}}\left(\boldsymbol{U}^+_{j+\frac12}-\boldsymbol{U}^-_{j+\frac12}-\boldsymbol{Q}_{j+\frac12}\right). \tag{2.2}$$

Here, $\boldsymbol{U}^{\pm}_{j+\frac12}$ are the right/left-sided values of a piecewise linear interpolant

$$\widetilde{\boldsymbol{U}}(x)=\overline{\boldsymbol{U}}_j+(\boldsymbol{U}_x)_j(x-x_j),\quad x\in C_j, \tag{2.3}$$

at the cell interface $x=x_{j+\frac12}$, namely

$$\boldsymbol{U}^-_{j+\frac12}=\overline{\boldsymbol{U}}_j+\frac{\Delta x}{2}(\boldsymbol{U}_x)_j,\quad \boldsymbol{U}^+_{j+\frac12}=\overline{\boldsymbol{U}}_{j+1}-\frac{\Delta x}{2}(\boldsymbol{U}_x)_{j+1}.$$

In order to ensure the non-oscillatory nature of this reconstruction, one needs to compute the slopes $(\boldsymbol{U}_x)_j$ in (2.3) using a nonlinear limiter. In all of the numerical experiments reported in §7, we have used a generalized minmod limiter [31,35,44]:

$$(\boldsymbol{U}_x)_j=\mathrm{minmod}\left(\theta\frac{\overline{\boldsymbol{U}}_j-\overline{\boldsymbol{U}}_{j-1}}{\Delta x},\ \frac{\overline{\boldsymbol{U}}_{j+1}-\overline{\boldsymbol{U}}_{j-1}}{2\Delta x},\ \theta\frac{\overline{\boldsymbol{U}}_{j+1}-\overline{\boldsymbol{U}}_j}{\Delta x}\right),\quad \theta\in[1,2], \tag{2.4}$$

applied in the component-wise manner. Here, the minmod function is defined as

$$\mathrm{minmod}(z_1,z_2,\ldots):=\begin{cases}\min_j\{z_j\} & \text{if } z_j>0\quad\forall\, j,\\ \max_j\{z_j\} & \text{if } z_j<0\quad\forall\, j,\\ 0 & \text{otherwise.}\end{cases}$$

The parameter θ in (2.4) can be used to control the amount of numerical viscosity present in the resulting scheme as the use of larger values of θ leads to less dissipative but more oscillatory reconstructions.

The term $\boldsymbol{Q}_{j+\frac12}$ in (2.2) represents a built-in "anti-diffusion" and it is given by (see [24]):

$$\boldsymbol{Q}_{j+\frac12}=\mathrm{minmod}\left(\boldsymbol{U}^+_{j+\frac12}-\boldsymbol{U}^*_{j+\frac12},\ \boldsymbol{U}^*_{j+\frac12}-\boldsymbol{U}^-_{j+\frac12}\right), \tag{2.5}$$

where

$$\boldsymbol{U}^*_{j+\frac12}=\frac{a^+_{j+\frac12}\boldsymbol{U}^+_{j+\frac12}-a^-_{j+\frac12}\boldsymbol{U}^-_{j+\frac12}-\left\{\boldsymbol{F}(\boldsymbol{U}^+_{j+\frac12})-\boldsymbol{F}(\boldsymbol{U}^-_{j+\frac12})\right\}}{a^+_{j+\frac12}-a^-_{j+\frac12}}. \tag{2.6}$$

Notice that the "anti-diffusion" term was switched off in [8], as the PCCU schemes presented there were based on the earlier version of the CU scheme from [25].

The one-sided local speeds of propagation $a^{\pm}_{j+\frac12}$ are estimated using the largest and the smallest eigenvalues of the Jacobian $A=\frac{\partial\boldsymbol{F}}{\partial\boldsymbol{U}}:\lambda_1(A)\le\ldots\le\lambda_N(A)$. This can be done, for example, by taking

$$\begin{aligned}a^+_{j+\frac12}&=\max\left\{\lambda_N\big(A(\boldsymbol{U}^+_{j+\frac12})\big),\lambda_N\big(A(\boldsymbol{U}^-_{j+\frac12})\big),0\right\},\\ a^-_{j+\frac12}&=\min\left\{\lambda_1\big(A(\boldsymbol{U}^+_{j+\frac12})\big),\lambda_1\big(A(\boldsymbol{U}^-_{j+\frac12})\big),0\right\}.\end{aligned} \tag{2.7}$$

Finally, the terms $\boldsymbol{B}_j$ and $\boldsymbol{B}_{\boldsymbol{\Psi},j+\frac12}$ in (2.1) reflect the contributions of the nonconservative products in the RHS of (1.1) and they are

$$\boldsymbol{B}_j := \int_{C_j} B\big(\widetilde{\boldsymbol{U}}(x)\big)\frac{\mathrm{d}\widetilde{\boldsymbol{U}}(x)}{\mathrm{d}x}\,\mathrm{d}x, \tag{2.8}$$

$$\boldsymbol{B}_{\boldsymbol{\Psi},j+\frac{1}{2}} := \int_0^1 B\big(\boldsymbol{\Psi}_{j+\frac{1}{2}}(s)\big)\frac{\mathrm{d}\boldsymbol{\Psi}_{j+\frac{1}{2}}(s)}{\mathrm{d}s}\,\mathrm{d}s, \tag{2.9}$$

where $\boldsymbol{\Psi}_{j+\frac{1}{2}}(s)$ is a path connecting the left- and right-side states $\boldsymbol{U}^-_{j+\frac{1}{2}}$ and $\boldsymbol{U}^+_{j+\frac{1}{2}}$ at the cell interface $x = x_{j+\frac{1}{2}}$. For details on evaluating (2.8) and (2.9), we refer the reader to [8].

3. 1-D fifth-order A-WENO schemes: a brief overview

In this section, we provide a brief overview of the A-WENO approach introduced in [20] (see also [32,33,46,48]), which has been proven to be a powerful tool for generalizing low-order FV schemes to higher-order FD ones.

Following [20], the point values $\boldsymbol{U}_j$ of the numerical solution of the conservative system (1.2) are evolved in time by solving the following system of ODEs:

$$\frac{\mathrm{d}\boldsymbol{U}_j}{\mathrm{d}t} = -\frac{\boldsymbol{\mathfrak{H}}_{\boldsymbol{j+\frac{1}{2}}} - \boldsymbol{\mathfrak{H}}_{\boldsymbol{j-\frac{1}{2}}}}{\Delta x}, \tag{3.1}$$

where $\boldsymbol{\mathfrak{H}}_{\boldsymbol{j+\frac{1}{2}}}$ is the (fifth-order accurate) numerical flux defined by

$$\boldsymbol{\mathfrak{H}}_{\boldsymbol{j+\frac{1}{2}}} = \boldsymbol{H}^{\mathrm{FV}}_{j+\frac{1}{2}} - \frac{1}{24}(\Delta x)^2(\boldsymbol{F}_{xx})_{j+\frac{1}{2}} + \frac{7}{5760}(\Delta x)^4(\boldsymbol{F}_{xxxx})_{j+\frac{1}{2}}. \tag{3.2}$$

Here, $\boldsymbol{H}^{\mathrm{FV}}_{j+\frac{1}{2}}$ is the FV numerical flux (for example, one may use the CU flux (2.2)), $(\boldsymbol{F}_{xx})_{j+\frac{1}{2}}$ and $(\boldsymbol{F}_{xxxx})_{j+\frac{1}{2}}$ are the higher-order correction terms computed by the fourth- and second-order accurate FDs, respectively:

$$\begin{aligned}
(\boldsymbol{F}_{xx})_{j+\frac{1}{2}} &= \frac{1}{48(\Delta x)^2}\left(-5\boldsymbol{F}_{j-2} + 39\boldsymbol{F}_{j-1} - 34\boldsymbol{F}_j - 34\boldsymbol{F}_{j+1} + 39\boldsymbol{F}_{j+2} - 5\boldsymbol{F}_{j+3}\right),\\
(\boldsymbol{F}_{xxxx})_{j+\frac{1}{2}} &= \frac{1}{2(\Delta x)^4}\left(\boldsymbol{F}_{j-2} - 3\boldsymbol{F}_{j-1} + 2\boldsymbol{F}_j + 2\boldsymbol{F}_{j+1} - 3\boldsymbol{F}_{j+2} + \boldsymbol{F}_{j+3}\right).
\end{aligned} \tag{3.3}$$

It should be emphasized that the resulting scheme (3.1)–(3.3) is fifth-order accurate once the one-sided point values $\boldsymbol{U}^{\pm}_{j+\frac{1}{2}}$ employed to compute the numerical flux $\boldsymbol{H}^{\mathrm{FV}}_{j+\frac{1}{2}}$ are fifth-order accurate. In order to achieve this, we apply the fifth-order WENO-Z interpolation to evaluate $\boldsymbol{U}^{\pm}_{j+\frac{1}{2}}$. For the sake of brevity, we present the details on the computation of the left-sided value $\boldsymbol{U}^-_{j+\frac{1}{2}}$, as $\boldsymbol{U}^+_{j+\frac{1}{2}}$ can be obtained using the mirror-symmetric stencil.

One can proceed with a component-wise approach. Then, for an i-th component of $\boldsymbol{U}_j$, the value $(U^{(i)}_{j+\frac{1}{2}})^-$ is calculated using a weighted average of the three parabolic interpolants $\mathcal{P}_0(x)$, $\mathcal{P}_1(x)$ and $\mathcal{P}_2(x)$ obtained using the stencils $[x_{j-2}, x_{j-1}, x_j]$, $[x_{j-1}, x_j, x_{j+1}]$ and $[x_j, x_{j+1}, x_{j+2}]$, respectively:

$$(U^{(i)}_{j+\frac{1}{2}})^- = \sum_{k=0}^{2}\omega^{(i)}_k\mathcal{P}^{(i)}_k(x_{j+\frac{1}{2}}), \tag{3.4}$$

where

$$\begin{aligned}
\mathcal{P}^{(i)}_0(x_{j+\frac{1}{2}}) &= \frac{3}{8}U^{(i)}_{j-2} - \frac{5}{4}U^{(i)}_{j-1} + \frac{15}{8}U^{(i)}_j,\\
\mathcal{P}^{(i)}_1(x_{j+\frac{1}{2}}) &= -\frac{1}{8}U^{(i)}_{j-1} + \frac{3}{4}U^{(i)}_j + \frac{3}{8}U^{(i)}_{j+1},\\
\mathcal{P}^{(i)}_2(x_{j+\frac{1}{2}}) &= \frac{3}{8}U^{(i)}_j + \frac{3}{4}U^{(i)}_{j+1} - \frac{1}{8}U^{(i)}_{j+2},
\end{aligned}$$

and the weights $\omega^{(i)}_k$ are computed by

$$\omega^{(i)}_k = \frac{\alpha^{(i)}_k}{\alpha^{(i)}_0 + \alpha^{(i)}_1 + \alpha^{(i)}_2}, \quad \alpha^{(i)}_k = d_k\left[1 + \left(\frac{\tau^{(i)}_5}{\beta^{(i)}_k + \varepsilon}\right)^p\right], \quad k = 0, 1, 2 \tag{3.5}$$

with $d_0 = \frac{1}{16}$, $d_1 = \frac{5}{8}$ and $d_2 = \frac{5}{16}$. The smoothness indicators $\beta^{(i)}_k$ for the corresponding parabolic interpolants $\mathcal{P}^{(i)}_k(x)$ are defined by

$$\beta_k^{(i)}=\sum_{\ell=1}^{2}(\Delta x)^{2\ell-1}\int\limits_{x_{j-\frac{1}{2}}}^{x_{j+\frac{1}{2}}}\left(\frac{\partial^\ell \mathcal{P}_k^{(i)}}{\partial x^\ell}\right)^2\mathrm{d}x,\quad k=0,1,2. \tag{3.6}$$

Evaluating the integrals in (3.6), we obtain

$$\begin{aligned}
\beta_0^{(i)}&=\frac{13}{12}\big(U_{j-2}^{(i)}-2U_{j-1}^{(i)}+U_j^{(i)}\big)^2+\frac{1}{4}\big(U_{j-2}^{(i)}-4U_{j-1}^{(i)}+3U_j^{(i)}\big)^2,\\
\beta_1^{(i)}&=\frac{13}{12}\big(U_{j-1}^{(i)}-2U_j^{(i)}+U_{j+1}^{(i)}\big)^2+\frac{1}{4}\big(U_{j-1}^{(i)}-U_{j+1}^{(i)}\big)^2,\\
\beta_2^{(i)}&=\frac{13}{12}\big(U_j^{(i)}-2U_{j+1}^{(i)}+U_{j+2}^{(i)}\big)^2+\frac{1}{4}\big(3U_j^{(i)}-4U_{j+1}^{(i)}+U_{j+2}^{(i)}\big)^2.
\end{aligned} \tag{3.7}$$

Finally, in formula (3.6), $\tau_5^{(i)}=\big|\beta_2^{(i)}-\beta_0^{(i)}\big|$, and in all of the numerical examples reported in §7, we have chosen $p=2$ and $\varepsilon=10^{-12}$.

Remark 3.1. It should be pointed out that the WENO-Z reconstruction applied in a component-wise manner may lead to oscillation in the computed solution; see, e.g., [40]. In order to minimize the magnitude of these oscillations, one may apply the WENO-Z interpolation procedure in the local characteristic variables using the local characteristic decomposition; see, e.g., [16,20,32,36,48].

4. 1-D fifth-order A-WENO PCCU schemes

In this section, we extend the second-order FV PCCU schemes reviewed in §2 to fifth-order A-WENO PCCU schemes. To this end, we first rewrite the nonconservative system (1.1) in the following form:

$$\boldsymbol{U}_t+\boldsymbol{K}(\boldsymbol{U})_x=\boldsymbol{0},$$

where

$$\boldsymbol{K}\big(\boldsymbol{U}(x,t)\big)=\boldsymbol{F}\big(\boldsymbol{U}(x,t)\big)-\int\limits^{x}B\big(\boldsymbol{U}(\xi,t)\big)\boldsymbol{U}_x(\xi,t)\,\mathrm{d}\xi$$

is a global flux. According to the A-WENO approach reviewed in §3, we substitute the PCCU numerical flux of $\boldsymbol{K}\big(\boldsymbol{U}(x,t)\big)$ into the A-WENO scheme (3.1), (3.2). This results in the fifth-order A-WENO PCCU scheme:

$$\begin{aligned}
\frac{\mathrm{d}\boldsymbol{U}_j}{\mathrm{d}t}=&-\frac{1}{\Delta x}\left[\boldsymbol{H}_{j+\frac{1}{2}}-\boldsymbol{H}_{j-\frac{1}{2}}-\boldsymbol{B}_j-\frac{a^+_{j-\frac{1}{2}}}{a^+_{j-\frac{1}{2}}-a^-_{j-\frac{1}{2}}}\boldsymbol{B}_{\boldsymbol{\Psi},j-\frac{1}{2}}+\frac{a^-_{j+\frac{1}{2}}}{a^+_{j+\frac{1}{2}}-a^-_{j+\frac{1}{2}}}\boldsymbol{B}_{\boldsymbol{\Psi},j+\frac{1}{2}}\right]\\
&+\frac{\Delta x}{24}\left[(\boldsymbol{K}_{xx})_{j+\frac{1}{2}}-(\boldsymbol{K}_{xx})_{j-\frac{1}{2}}\right]-\frac{7}{5760}(\Delta x)^3\left[(\boldsymbol{K}_{xxxx})_{j+\frac{1}{2}}-(\boldsymbol{K}_{xxxx})_{j-\frac{1}{2}}\right],
\end{aligned} \tag{4.1}$$

where $\boldsymbol{H}_{j+\frac{1}{2}}$ is defined in (2.2), (2.5), (2.6), $a^\pm_{j+\frac{1}{2}}$ are given by (2.7), and $\boldsymbol{U}^\pm_{j+\frac{1}{2}}$ are computed using the fifth-order WENO-Z interpolation described in §3. In addition, $(\boldsymbol{K}_{xx})_{j+\frac{1}{2}}$ and $(\boldsymbol{K}_{xxxx})_{j+\frac{1}{2}}$ are approximations of the second- and fourth-order spatial derivatives of $\boldsymbol{K}\big(\boldsymbol{U}(x,t)\big)$, given by

$$\begin{aligned}
(\boldsymbol{K}_{xx})_{j+\frac{1}{2}}&=(\boldsymbol{F}_{xx})_{j+\frac{1}{2}}-\big[(B(\boldsymbol{U})\boldsymbol{U}_x)_x\big]_{j+\frac{1}{2}},\\
(\boldsymbol{K}_{xxxx})_{j+\frac{1}{2}}&=(\boldsymbol{F}_{xxxx})_{j+\frac{1}{2}}-\big[(B(\boldsymbol{U})\boldsymbol{U}_x)_{xxx}\big]_{j+\frac{1}{2}},
\end{aligned}$$

where $(\boldsymbol{F}_{xx})_{j+\frac{1}{2}}$ and $(\boldsymbol{F}_{xxxx})_{j+\frac{1}{2}}$ are computed using (3.3). For approximating $\big[(B(\boldsymbol{U})\boldsymbol{U}_x)_x\big]_{j+\frac{1}{2}}$ and $\big[(B(\boldsymbol{U})\boldsymbol{U}_x)_{xxx}\big]_{j+\frac{1}{2}}$, we use FDs to obtain

$$\begin{aligned}
\big[(B(\boldsymbol{U})\boldsymbol{U}_x)_x\big]_{j+\frac{1}{2}}&=\frac{1}{24\Delta x}\Big[-(B(\boldsymbol{U})\boldsymbol{U}_x)_{j+2}+27(B(\boldsymbol{U})\boldsymbol{U}_x)_{j+1}\\
&\qquad-27(B(\boldsymbol{U})\boldsymbol{U}_x)_j+(B(\boldsymbol{U})\boldsymbol{U}_x)_{j-1}\Big],\\
\big[(B(\boldsymbol{U})\boldsymbol{U}_x)_{xxx}\big]_{j+\frac{1}{2}}&=\frac{1}{(\Delta x)^3}\Big[(B(\boldsymbol{U})\boldsymbol{U}_x)_{j+2}-3(B(\boldsymbol{U})\boldsymbol{U}_x)_{j+1}\\
&\qquad+3(B(\boldsymbol{U})\boldsymbol{U}_x)_j-(B(\boldsymbol{U})\boldsymbol{U}_x)_{j-1}\Big].
\end{aligned}$$

Here, $(B(\boldsymbol{U})\boldsymbol{U}_x)_m = B(\boldsymbol{U}_m)(\boldsymbol{U}_x)_m$ for $m = j-1,\ j,\ j+1,\ j+2$, and

$$
\begin{aligned}
(\boldsymbol{U}_x)_{j-1} &= \frac{1}{12\Delta x}\left(\boldsymbol{U}_{j+2} - 6\boldsymbol{U}_{j+1} + 18\boldsymbol{U}_j - 10\boldsymbol{U}_{j-1} - 3\boldsymbol{U}_{j-2}\right),\\
(\boldsymbol{U}_x)_{j} &= \frac{1}{12\Delta x}\left(-\boldsymbol{U}_{j+2} + 8\boldsymbol{U}_{j+1} - 8\boldsymbol{U}_{j-1} + \boldsymbol{U}_{j-2}\right),\\
(\boldsymbol{U}_x)_{j+1} &= \frac{1}{12\Delta x}\left(-\boldsymbol{U}_{j+3} + 8\boldsymbol{U}_{j+2} - 8\boldsymbol{U}_{j} + \boldsymbol{U}_{j-1}\right),\\
(\boldsymbol{U}_x)_{j+2} &= \frac{1}{12\Delta x}\left(3\boldsymbol{U}_{j+3} + 10\boldsymbol{U}_{j+2} - 18\boldsymbol{U}_{j+1} + 6\boldsymbol{U}_{j} - \boldsymbol{U}_{j-1}\right).
\end{aligned}
$$

Next, the integral in $\boldsymbol{B}_{\boldsymbol{\Psi},j+\frac{1}{2}}$ is computed using a linear segment path

$$
\boldsymbol{\Psi}_{j+\frac{1}{2}}(s) = \boldsymbol{U}^-_{j+\frac{1}{2}} + s(\boldsymbol{U}^+_{j+\frac{1}{2}} - \boldsymbol{U}^-_{j+\frac{1}{2}}), \tag{4.2}
$$

which we substitute into (2.9); see, for example, a particular formula (6.4) computed for the two-layer shallow water system studied in §6. We note that when the point values $\boldsymbol{U}^{\pm}_{j+\frac{1}{2}}$ are fifth-order accurate, the RHS of (4.1) will be fifth-order accurate provided the term $\boldsymbol{B}_j$ is evaluated using a fifth-order quadrature. One can see that this cannot be done using formula (2.8) as in the A-WENO approach we do not reconstruct piecewise polynomial approximations $\widetilde{\boldsymbol{U}}$, which are uniformly fifth-order accurate in the entire cell C_j. Instead, we develop a special fifth-order A-WENO quadrature for the integrals of nonconservative terms $\int_{C_j}\sigma\phi_x\,\mathrm{d}x$, where $\sigma := b_{m\ell}(\boldsymbol{U})$ and $\phi := U^{(\ell)}$, appearing on the RHS of the nonconservative system (1.1). To this end, we use the Newton-Cotes approach based on the five points $x_{j-\frac{1}{2}}$, $x_{j-\frac{1}{4}}$, x_j, $x_{j+\frac{1}{4}}$, $x_{j+\frac{1}{2}}$ and the corresponding values of $\boldsymbol{U}$ at these points: $\boldsymbol{U}^+_{j-\frac{1}{2}}$, $\boldsymbol{U}_{j-\frac{1}{4}}$, $\boldsymbol{U}_j$, $\boldsymbol{U}_{j+\frac{1}{4}}$ and $\boldsymbol{U}^-_{j+\frac{1}{2}}$. The values $\boldsymbol{U}^+_{j-\frac{1}{2}}$ and $\boldsymbol{U}^-_{j+\frac{1}{2}}$ are obtained using the WENO-Z interpolant; see §3. The values $\boldsymbol{U}_{j-\frac{1}{4}}$ and $\boldsymbol{U}_{j+\frac{1}{4}}$ are also computed using the WENO-Z interpolant. Here, we show how to obtain $\boldsymbol{U}_{j-\frac{1}{4}}$ as $\boldsymbol{U}_{j+\frac{1}{4}}$ can be calculated using the mirror-symmetric stencil.

For each component of $\boldsymbol{U}_{j-\frac{1}{4}}$, the value of $U^{(i)}_{j-\frac{1}{4}}$ is calculated using a weighted average of the same three parabolic interpolants $\mathcal{P}_0$, $\mathcal{P}_1$ and $\mathcal{P}_2$ as in (3.4) so that

$$
U^{(i)}_{j-\frac{1}{4}} = \sum_{k=0}^{2}\omega^{(i)}_k\mathcal{P}^{(i)}_k(x_{j-\frac{1}{4}}),
$$

where

$$
\begin{aligned}
\mathcal{P}^{(i)}_0(x_{j-\frac{1}{4}}) &= -\frac{3}{32}U^{(i)}_{j-2} + \frac{7}{16}U^{(i)}_{j-1} + \frac{21}{32}U^{(i)}_{j},\\
\mathcal{P}^{(i)}_1(x_{j-\frac{1}{4}}) &= \frac{5}{32}U^{(i)}_{j-1} + \frac{15}{16}U^{(i)}_{j} - \frac{3}{32}U^{(i)}_{j+1},\\
\mathcal{P}^{(i)}_2(x_{j-\frac{1}{4}}) &= \frac{45}{32}U^{(i)}_{j} - \frac{9}{16}U^{(i)}_{j+1} + \frac{5}{32}U^{(i)}_{j+2}.
\end{aligned}
$$

As in §3, the weights $\omega^{(i)}_k$ are computed by (3.5), but with $d_0 = \frac{15}{64}$, $d_1 = \frac{21}{32}$ and $d_2 = \frac{7}{64}$. The smoothness indicators $\beta^{(i)}_k$ are still computed by (3.7) and $\tau^{(i)}_5 = |\beta^{(i)}_2 - \beta^{(i)}_0|$.

Equipped with the point values of $\sigma_k := b_{m\ell}(\boldsymbol{U}_k)$ and $\phi_k = U^{(\ell)}_k$, $k = j\pm\frac{1}{2}, j\pm\frac{1}{4}, j$, we construct a fourth-degree interpolating polynomials in every cell. This results in piecewise polynomials $\widetilde{\sigma}(x)$ and $\widetilde{\phi}(x)$, for which we have

$$
\begin{aligned}
\widetilde{\sigma}(x) = \frac{1}{3(\Delta x)^4}\Big[&3(\Delta x)^4\sigma_j + (\Delta x)^3\big(\sigma^+_{j-\frac{1}{2}} - 8\sigma_{j-\frac{1}{4}} + 8\sigma_{j+\frac{1}{4}} - \sigma^-_{j+\frac{1}{2}}\big)(x-x_j)\\
&- 2(\Delta x)^2\big(\sigma^+_{j-\frac{1}{2}} - 16\sigma_{j-\frac{1}{4}} + 30\sigma_j - 16\sigma_{j+\frac{1}{4}} + \sigma^-_{j+\frac{1}{2}}\big)(x-x_j)^2\\
&- 16\Delta x\big(\sigma^+_{j-\frac{1}{2}} - 2\sigma_{j-\frac{1}{4}} + 2\sigma_{j+\frac{1}{4}} - \sigma^-_{j+\frac{1}{2}}\big)(x-x_j)^3\\
&+ 32\big(\sigma^+_{j-\frac{1}{2}} - 4\sigma_{j-\frac{1}{4}} + 6\sigma_j - 4\sigma_{j+\frac{1}{4}} + \sigma^-_{j+\frac{1}{2}}\big)(x-x_j)^4\Big], \quad x\in C_j,
\end{aligned} \tag{4.3}
$$

$$\begin{aligned}\widetilde{\phi}_x(x)=\frac{1}{3(\Delta x)^4}\Big[&(\Delta x)^3\big(\phi^+_{j-\frac12}-8\phi_{j-\frac14}+8\phi_{j+\frac14}-\phi^-_{j+\frac12}\big)\\&-4(\Delta x)^2\big(\phi^+_{j-\frac12}-16\phi_{j-\frac14}+30\phi_j-16\phi_{j+\frac14}+u^-_{j+\frac12}\big)(x-x_j)\\&-48\Delta x\big(\phi^+_{j-\frac12}-2\phi_{j-\frac14}+2\phi_{j+\frac14}-\phi^-_{j+\frac12}\big)(x-x_j)^2\\&+128\big(\phi^+_{j-\frac12}-4\phi_{j-\frac14}+6\phi_j-4\phi_{j+\frac14}+\phi^-_{j+\frac12}\big)(x-x_j)^3\Big],\quad x\in C_j.\end{aligned}$$

We then use (4.3) to approximate

$$\begin{aligned}\int_{C_j}\sigma\phi_x\,\mathrm{d}x\approx\int_{C_j}\widetilde{\sigma}(x)\widetilde{\phi}_x(x)\,\mathrm{d}x=\frac{1}{1890}\Big[&107(\sigma^-_{j+\frac12}\phi^+_{j-\frac12}-\sigma^+_{j-\frac12}\phi^-_{j+\frac12})\\&+2112\big\{(\sigma_{j-\frac14}-\sigma_{j+\frac14})\phi_j+(\phi_{j+\frac14}-\phi_{j-\frac14})\sigma_j\big\}+1024\big(\sigma_{j+\frac14}\phi_{j-\frac14}-\sigma_{j-\frac14}\phi_{j+\frac14}\big)\\&+804\big\{(\sigma^-_{j+\frac12}-\sigma^+_{j-\frac12})\phi_j+(\phi^+_{j-\frac12}-\phi^-_{j+\frac12})\sigma_j\big\}+945\big(\sigma^-_{j+\frac12}\phi^-_{j+\frac12}-\sigma^+_{j-\frac12}\phi^+_{j-\frac12}\big)\\&+1472\big(\sigma_{j+\frac14}\phi^-_{j+\frac12}-\sigma^-_{j+\frac12}\phi_{j+\frac14}+\sigma^+_{j-\frac12}\phi_{j-\frac14}-\sigma_{j-\frac14}\phi^+_{j-\frac12}\big)\\&+384\big(\sigma_{j-\frac14}\phi^-_{j+\frac12}+\sigma^+_{j-\frac12}\phi_{j+\frac14}-\sigma^-_{j+\frac12}\phi_{j-\frac14}-\sigma_{j+\frac14}\phi^+_{j-\frac12}\big)\Big].\end{aligned}\tag{4.4}$$

Remark 4.1. It is easy to show that the quadrature (4.4) is fifth-order accurate for sufficiently smooth σ and ϕ.

5. 2-D fifth-order A-WENO PCCU schemes

In this section, we generalize the 1-D fifth-order A-WENO PCCU schemes for the 2-D nonconservative systems, which read as

$$\boldsymbol{U}_t+\boldsymbol{F}(\boldsymbol{U})_x+\boldsymbol{G}(\boldsymbol{U})_y=B(\boldsymbol{U})\boldsymbol{U}_x+C(\boldsymbol{U})\boldsymbol{U}_y.\tag{5.1}$$

To this end, we take an advantage of the A-WENO approach and design the 2-D scheme in a "dimension-by-dimension" manner.

We first rewrite the 2-D nonconservative system in the quasi-conservative form:

$$\boldsymbol{U}_t+\boldsymbol{K}(\boldsymbol{U})_x+\boldsymbol{L}(\boldsymbol{U})_y=\boldsymbol{0},$$

where

$$\begin{aligned}\boldsymbol{K}(\boldsymbol{U}(x,y,t))&=\boldsymbol{F}(\boldsymbol{U}(x,y,t))-\int^x B\big(\boldsymbol{U}(\xi,y,t)\big)\boldsymbol{U}_x(\xi,y,t)\,\mathrm{d}\xi,\\\boldsymbol{L}(\boldsymbol{U}(x,y,t))&=\boldsymbol{G}(\boldsymbol{U}(x,y,t))-\int^y C\big(\boldsymbol{U}(x,\eta,t)\big)\boldsymbol{U}_y(x,\eta,t)\,\mathrm{d}\eta,\end{aligned}$$

are global fluxes. The 2-D A-WENO PCCU scheme is then obtained precisely as its 1-D prototype constructed in §4, and it reads as (compare with (4.1))

$$\begin{aligned}\frac{\mathrm{d}\boldsymbol{U}_{j,k}}{\mathrm{d}t}=&-\frac{1}{\Delta x}\left[\boldsymbol{H}^x_{j+\frac12,k}-\boldsymbol{H}^x_{j-\frac12,k}-\boldsymbol{B}_{j,k}-\frac{a^+_{j-\frac12,k}}{a^+_{j-\frac12,k}-a^-_{j-\frac12,k}}\boldsymbol{B}_{\boldsymbol{\Psi},j-\frac12,k}+\frac{a^-_{j+\frac12,k}}{a^+_{j+\frac12,k}-a^-_{j+\frac12,k}}\boldsymbol{B}_{\boldsymbol{\Psi},j+\frac12,k}\right]\\&+\frac{\Delta x}{24}\left[(\boldsymbol{K}_{xx})_{j+\frac12,k}-(\boldsymbol{K}_{xx})_{j-\frac12,k}\right]-\frac{7}{5760}(\Delta x)^3\left[(\boldsymbol{K}_{xxxx})_{j+\frac12,k}-(\boldsymbol{K}_{xxxx})_{j-\frac12,k}\right]\\&-\frac{1}{\Delta y}\left[\boldsymbol{H}^y_{j,k+\frac12}-\boldsymbol{H}^y_{j,k-\frac12}-\boldsymbol{C}_{j,k}-\frac{a^+_{j,k-\frac12}}{a^+_{j,k-\frac12}-a^-_{j,k-\frac12}}\boldsymbol{C}_{\boldsymbol{\Psi},j,k-\frac12}+\frac{a^-_{j,k+\frac12}}{a^+_{j,k+\frac12}-a^-_{j,k+\frac12}}\boldsymbol{C}_{\boldsymbol{\Psi},j,k+\frac12}\right]\\&+\frac{\Delta y}{24}\left[(\boldsymbol{L}_{yy})_{j,k+\frac12}-(\boldsymbol{L}_{yy})_{j,k-\frac12}\right]-\frac{7}{5760}(\Delta y)^3\left[(\boldsymbol{L}_{yyyy})_{j,k+\frac12}-(\boldsymbol{L}_{yyyy})_{j,k-\frac12}\right].\end{aligned}\tag{5.2}$$

All of the terms in (5.2) are computed as in §4 separately in the x- and y-directions. We omit the details for the sake of brevity.

6. Applications to two-layer shallow water equations

In this section, we show the applications of the developed fifth-order A-WENO PCCU schemes introduced in §4 and §5 to the two-layer shallow water equations.

6.1. 1-D two-layer shallow water equations

We begin with the 1-D two-layer shallow water equations, which read as

$$\begin{aligned}
&(h_1)_t + (q_1)_x = 0,\\
&(q_1)_t + \Big(h_1u_1^2 + \frac{g}{2}h_1^2\Big)_x = -gh_1Z_x - gh_1(h_2)_x,\\
&(h_2)_t + (q_2)_x = 0,\\
&(q_2)_t + \Big(h_2u_2^2 + \frac{g}{2}h_2^2\Big)_x = -gh_2Z_x - grh_2(h_1)_x,
\end{aligned} \tag{6.1}$$

where h_1 and h_2 are the depths of the upper and lower layers of the flow, respectively, u_i and $q_i = h_iu_i$, $i = 1, 2$ are the corresponding velocities and discharges, $Z(x)$ represents the time-independent bottom topography, g is the acceleration due to gravity, and $r := \frac{\rho_1}{\rho_2} < 1$ is the constant density ratio of the two layers.

Our goal is to develop a well-balanced fifth-order A-WENO PCCU scheme for the two-layer system (6.1). In general, schemes are called well-balanced when they are capable of preserving (several) steady-state solutions of the studied system within a machine accuracy; see, e.g., [3,22] and references therein. It is known that the main advantage of well-balanced schemes is that they can accurately capture small perturbations of such steady state even when a coarse mesh is used. This makes a well-balanced property practically important.

It is easy to check that the system (6.1) admits the following family of smooth steady-state solutions:

$$q_1 \equiv \texttt{Const}, \quad q_2 \equiv \texttt{Const}, \quad \frac{u_1^2}{2} + g(w + h_1) \equiv \texttt{Const}, \quad \frac{u_2^2}{2} + g(w + rh_1) \equiv \texttt{Const},$$

where $w := h_2 + Z$ represents the interface between the upper and lower layers. Particular steady states that belong to this family of equilibria are so-called "lake-at-rest" states:

$$u_1 = u_2 \equiv 0, \quad h_1 \equiv \texttt{Const}, \quad w \equiv \texttt{Const}. \tag{6.2}$$

We note that these steady states are practically important as many physically relevant solutions are, in fact, small perturbations of (6.2). The A-WENO PCCU schemes we present below are well-balanced in the sense that they are capable of exactly preserving (6.2).

In order to derive the well-balanced scheme, we first follow the idea from [23] (see also [26]) and rewrite the system (6.1) in terms of the equilibrium variables h_1, q_1, w and q_2, which are constant at "lake-at-rest" steady states. The rewritten system reads as

$$\begin{aligned}
&(h_1)_t + (q_1)_x = 0,\\
&(q_1)_t + \Big(\frac{q_1^2}{h_1} + \frac{g}{2}h_1^2\Big)_x = -gh_1w_x,\\
&(w)_t + (q_2)_x = 0,\\
&(q_2)_t + \Big(\frac{q_2^2}{w - Z} + \frac{g}{2}w^2\Big)_x = gZw_x - gr(w - Z)(h_1)_x.
\end{aligned} \tag{6.3}$$

It is easy to verify that the systems (6.1) and (6.3) are equivalent for smooth solutions. We also note that the second-order PCCU schemes applied to (6.1) and (6.3) are equivalent. This can be proved along the lines of [8, §4.2.2], where the equivalence of the second-order PCCU schemes for (6.1) and its equivalent formulation [8, (4.25)] were shown.

We now write the system (6.3) in the vector form (1.1) with $\boldsymbol{U} = (h_1, q_1, w, q_2)^\top$, $\boldsymbol{F}(\boldsymbol{U}) = (q_1, \frac{q_1^2}{h_1} + \frac{g}{2}h_1^2, q_2, \frac{q_2^2}{w-Z} + \frac{g}{2}w^2)^\top$, and

$$B(\boldsymbol{U}) = \begin{pmatrix} 0 & 0 & 0 & 0\\ 0 & 0 & -gh_1 & 0\\ 0 & 0 & 0 & 0\\ -gr(w - Z) & 0 & gZ & 0 \end{pmatrix}.$$

Applying the 1-D fifth-order A-WENO PCCU scheme introduced in §4 to the system (6.3), we arrive at the semi-discretization (4.1) with the integral terms in

$$\boldsymbol{B}_j \approx \Big(0, -\int\limits_{C_j} g h_1 w_x \,\mathrm{d}x, 0, -\int\limits_{C_j} \big[gr(w-Z)(h_1)_x - gZ w_x\big]\,\mathrm{d}x\Big)^\top$$

approximated by (4.4), the upper (lower) bounds on one-sided local speeds, $a^+_{j+\frac12}$ ($a^-_{j+\frac12}$) obtained using the Lagrange theorem precisely as described in [26, §2.3], and $\boldsymbol{B}_{\boldsymbol{\Psi},j+\frac12} = \big(B^{(1)}_{\boldsymbol{\Psi},j+\frac12},\ldots,B^{(4)}_{\boldsymbol{\Psi},j+\frac12}\big)^\top$ evaluated using the linear segment path (4.2), which results in

$$\begin{aligned}
&B^{(1)}_{\boldsymbol{\Psi},j+\frac12} = B^{(3)}_{\boldsymbol{\Psi},j+\frac12} = 0, \quad B^{(2)}_{\boldsymbol{\Psi},j+\frac12} = -\frac{g}{2}\big((h_1)^+_{j+\frac12} + (h_1)^-_{j+\frac12}\big)\big(w^+_{j+\frac12} - w^-_{j+\frac12}\big)\\
&B^{(4)}_{\boldsymbol{\Psi},j+\frac12} = -\frac{gr}{2}\big(w^+_{j+\frac12} - Z^+_{j+\frac12} + w^-_{j+\frac12} - Z^-_{j+\frac12}\big)\big((h_1)^+_{j+\frac12} - (h_1)^-_{j+\frac12}\big),\\
&\qquad\qquad + \frac{g}{2}\big(Z^+_{j+\frac12} + Z^-_{j+\frac12}\big)\big(w^+_{j+\frac12} - w^-_{j+\frac12}\big).
\end{aligned} \tag{6.4}$$

Remark 6.1. Note that the time-independent values $Z^\pm_{j+\frac12}$ are obtained separately by applying the same WENO-Z interpolation to Z, which is, however, performed only once in the beginning of the time evolution process.

Remark 6.2. In all of the numerical examples presented in §7, we have implemented the WENO-Z interpolation procedure using the local characteristic variables, which are obtained using the local characteristic decomposition as follows.

In order to evaluate the point values $\boldsymbol{U}^\pm_{j+\frac12}$, we first introduce the matrix

$$\begin{aligned}
\mathcal{A}_{j+\frac12} &= A(\widehat{\boldsymbol{U}}_{j+\frac12}) - B(\widehat{\boldsymbol{U}}_{j+\frac12})\\
&= \begin{pmatrix}
0 & 1 & 0 & 0\\
g(\hat{h}_1)_{j+\frac12} - (\hat{u}_1)^2_{j+\frac12} & 2(\hat{u}_1)_{j+\frac12} & g(\hat{h}_1)_{j+\frac12} & 0\\
0 & 0 & 0 & 1\\
gr(\hat{h}_2)_{j+\frac12} & 0 & g(\hat{h}_2)_{j+\frac12} - (\hat{u}_2)^2_{j+\frac12} & 2(\hat{u}_2)_{j+\frac12}
\end{pmatrix},
\end{aligned}$$

where, as before, $A = \frac{\partial \boldsymbol{F}}{\partial \boldsymbol{U}}$, and $\widehat{(\cdot)}$ stands for the following Roe averages [9]:

$$\begin{aligned}
&(\hat{h}_1)_{j+\frac12} = \frac{(h_1)_j + (h_1)_{j+1}}{2}, \quad (\hat{u}_1)_{j+\frac12} = \frac{\sqrt{(h_1)_j}(u_1)_j + \sqrt{(h_1)_{j+1}}(u_1)_{j+1}}{\sqrt{(h_1)_j} + \sqrt{(h_1)_{j+1}}},\\
&(\hat{h}_2)_{j+\frac12} = \frac{(h_2)_j + (h_2)_{j+1}}{2}, \quad (\hat{u}_2)_{j+\frac12} = \frac{\sqrt{(h_2)_j}(u_2)_j + \sqrt{(h_2)_{j+1}}(u_2)_{j+1}}{\sqrt{(h_2)_j} + \sqrt{(h_2)_{j+1}}},
\end{aligned}$$

where $(h_2)_j := w_j - Z_j$. We then numerically compute the matrices $R_{j+\frac12}$ and $R^{-1}_{j+\frac12}$ such that $R^{-1}_{j+\frac12}\widehat{A}_{j+\frac12}R_{j+\frac12}$ is a diagonal matrix, and introduce the local characteristic variables in the neighborhood of $x = x_{j+\frac12}$:

$$\boldsymbol{\Gamma}_k = R^{-1}_{j+\frac12}\boldsymbol{U}_k, \quad k = j-2,\ldots,j+3.$$

Finally, we apply the WENO-Z interpolation to these six values of $\boldsymbol{\Gamma}$, obtain the point values $\boldsymbol{\Gamma}^\pm_{j+\frac12}$, and then end up with

$$\boldsymbol{U}^\pm_{j+\frac12} = R_{j+\frac12}\boldsymbol{\Gamma}^\pm_{j+\frac12}.$$

6.2. 2-D two-layer shallow water equations

In this section, we show the application of the 2-D fifth-order A-WENO PCCU scheme introduced in §5 to the 2-D two-layer shallow water equations, which read as

$$
\begin{aligned}
&(h_1)_t + (q_1)_x + (p_1)_y = 0,\\
&(q_1)_t + \Big(h_1u_1^2 + \frac{g}{2}h_1^2\Big)_x + (h_1u_1v_1)_y = -gh_1Z_x - gh_1(h_2)_x,\\
&(p_1)_t + (h_1u_1v_1)_x + \Big(h_1v_1^2 + \frac{g}{2}h_1^2\Big)_y = -gh_1Z_y - gh_1(h_2)_y,\\
&(h_2)_t + (q_2)_x + (p_2)_y = 0,\\
&(q_2)_t + \Big(h_2u_2^2 + \frac{g}{2}h_2^2\Big)_x + (h_2u_2v_2)_y = -gh_2Z_x - grh_2(h_1)_x,\\
&(p_2)_t + (h_2u_2v_2)_x + \Big(h_2v_2^2 + \frac{g}{2}h_2^2\Big)_y = -gh_2Z_y - grh_2(h_1)_y,
\end{aligned}
\tag{6.5}
$$

where v_i and $p_i = h_iv_i$, $i = 1, 2$ are the y-velocities and y-discharges, respectively, and the rest of the notations are the same as in the 1-D case.

As in the 1-D case, in order to develop a well-balanced fifth-order A-WENO PCCU scheme, which is capable of exactly preserving "lake-at-rest" steady-state solutions satisfying

$$
u_1 = u_2 = v_1 = v_2 \equiv 0, \quad h_1 \equiv \texttt{Const}, \quad w \equiv \texttt{Const},
$$

we rewrite the system (6.5) in terms of the equilibrium variables h_1, q_1, p_1, w, q_2 and p_2. The new system reads as

$$
\begin{aligned}
&(h_1)_t + (q_1)_x + (p_1)_y = 0,\\
&(q_1)_t + \Big(\frac{q_1^2}{h_1} + \frac{g}{2}h_1^2\Big)_x + \Big(\frac{p_1q_1}{h_1}\Big)_y = -gh_1w_x,\\
&(p_1)_t + \Big(\frac{p_1q_1}{h_1}\Big)_x + \Big(\frac{p_1^2}{h_1} + \frac{g}{2}h_1^2\Big)_y = -gh_1w_y,\\
&(w)_t + (q_2)_x + (p_2)_y = 0,\\
&(q_2)_t + \Big(\frac{q_2^2}{w-Z} + \frac{g}{2}w^2\Big)_x + \Big(\frac{p_2q_2}{w-Z}\Big)_y = gZw_x - gr(w-Z)(h_1)_x,\\
&(p_2)_t + \Big(\frac{p_2q_2}{w-Z}\Big)_x + \Big(\frac{p_2^2}{w-Z} + \frac{g}{2}w^2\Big)_y = gZw_y - gr(w-Z)(h_1)_y.
\end{aligned}
\tag{6.6}
$$

This systems can be written in the vector form (5.1) with $\boldsymbol{U} = \big(h_1, q_1, p_1, w, q_2, p_2\big)^\top$, $\boldsymbol{F}(\boldsymbol{U}) = \big(q_1, \frac{q_1^2}{h_1} + \frac{g}{2}h_1^2, \frac{p_1q_1}{h_1}, q_2, \frac{q_2^2}{w-Z} + \frac{g}{2}w^2, \frac{p_2q_2}{w-Z}\big)^\top$, $\boldsymbol{G}(\boldsymbol{U}) = \big(p_1, \frac{p_1q_1}{h_1}, \frac{p_1^2}{h_1} + \frac{g}{2}h_1^2, p_2, \frac{p_2q_2}{w-Z}, \frac{p_2^2}{w-Z} + \frac{g}{2}w^2\big)^\top$,

$$
B(\boldsymbol{U}) = \begin{pmatrix}
0 & 0 & 0 & 0 & 0 & 0\\
0 & 0 & 0 & -gh_1 & 0 & 0\\
0 & 0 & 0 & 0 & 0 & 0\\
0 & 0 & 0 & 0 & 0 & 0\\
-gr(w-Z) & 0 & 0 & gZ & 0 & 0\\
0 & 0 & 0 & 0 & 0 & 0
\end{pmatrix}, \quad
C(\boldsymbol{U}) = \begin{pmatrix}
0 & 0 & 0 & 0 & 0 & 0\\
0 & 0 & 0 & 0 & 0 & 0\\
0 & 0 & 0 & -gh_1 & 0 & 0\\
0 & 0 & 0 & 0 & 0 & 0\\
0 & 0 & 0 & 0 & 0 & 0\\
-gr(w-Z) & 0 & 0 & gZ & 0 & 0
\end{pmatrix}.
$$

Applying the 2-D fifth-order A-WENO PCCU scheme introduced in §5 to the system (6.6), the point values of its solution are evolved in time by solving the ODE system (5.2) with the integrals in the nonconservative product terms,

$$
\begin{aligned}
\boldsymbol{B}_{j,k} \approx \Bigg(&0, -\int\limits_{x_{j-\frac12}}^{x_{j+\frac12}} gh_1(x, y_k)(w(x, y_k))_x\,\mathrm{d}x, 0,\\
&0, -\int\limits_{x_{j-\frac12}}^{x_{j+\frac12}} \Big[gr\big(w(x, y_k) - Z(x, y_k)\big)(h_1(x, y_k))_x - gZ(x, y_k)(w(x, y_k))_x\Big]\mathrm{d}x, 0\Bigg)^\top
\end{aligned}
$$

and

$$\boldsymbol{C}_{j,k} \approx \Bigg(0, 0, -\int\limits_{y_{k-\frac{1}{2}}}^{y_{k+\frac{1}{2}}} gh_1(x_j, y)(w(x_j, y))_y \,\mathrm{d}y,$$
$$0, 0, -\int\limits_{y_{k-\frac{1}{2}}}^{y_{k+\frac{1}{2}}} \Big[gr\big(w(x_j, y) - Z(x_j, y)\big)(h_1(x_j, y))_y - gZ(x_j, y)(w(x_j, y))_y\Big]\mathrm{d}y\Bigg)^\top$$

approximated by the 1-D fifth-order quadrature (4.4), $\boldsymbol{B}_{\boldsymbol{\Psi},j+\frac{1}{2},k}$ evaluated using the linear segment path connecting $\boldsymbol{U}^-_{j+\frac{1}{2},k}$ with $\boldsymbol{U}^+_{j+\frac{1}{2},k}$:

$$\boldsymbol{\Psi}_{j+\frac{1}{2},k}(s) = \boldsymbol{U}^-_{j+\frac{1}{2},k} + s\big(\boldsymbol{U}^+_{j+\frac{1}{2},k} - \boldsymbol{U}^-_{j+\frac{1}{2},k}\big),$$

and $\boldsymbol{C}_{\boldsymbol{\Psi},j,k+\frac{1}{2}}$ computed with the help of the linear segment path connecting $\boldsymbol{U}^-_{j,k+\frac{1}{2}}$ with $\boldsymbol{U}^+_{j,k+\frac{1}{2}}$:

$$\boldsymbol{\Psi}_{j,k+\frac{1}{2}}(s) = \boldsymbol{U}^-_{j,k+\frac{1}{2}} + s\big(\boldsymbol{U}^+_{j,k+\frac{1}{2}} - \boldsymbol{U}^-_{j,k+\frac{1}{2}}\big).$$

Applying the above two paths, we obtain $\boldsymbol{B}_{\boldsymbol{\Psi},j+\frac{1}{2},k} = \big(B^{(1)}_{\boldsymbol{\Psi},j+\frac{1}{2},k}, \ldots, B^{(6)}_{\boldsymbol{\Psi},j+\frac{1}{2},k}\big)^\top$ and $\boldsymbol{C}_{\boldsymbol{\Psi},j,k+\frac{1}{2}} = \big(C^{(1)}_{\boldsymbol{\Psi},j,k+\frac{1}{2}}, \ldots, C^{(6)}_{\boldsymbol{\Psi},j,k+\frac{1}{2}}\big)^\top$, where

$$\begin{aligned}
&B^{(1)}_{\boldsymbol{\Psi},j+\frac{1}{2},k} = B^{(3)}_{\boldsymbol{\Psi},j+\frac{1}{2},k} = B^{(4)}_{\boldsymbol{\Psi},j+\frac{1}{2},k} = B^{(6)}_{\boldsymbol{\Psi},j+\frac{1}{2},k} = 0,\\
&B^{(2)}_{\boldsymbol{\Psi},j+\frac{1}{2},k} = -\frac{g}{2}\big((h_1)^+_{j+\frac{1}{2},k} + (h_1)^-_{j+\frac{1}{2},k}\big)\big(w^+_{j+\frac{1}{2},k} - w^-_{j+\frac{1}{2},k}\big),\\
&B^{(5)}_{\boldsymbol{\Psi},j+\frac{1}{2},k} = \Big[-\frac{gr}{2}\big(w^+_{j+\frac{1}{2},k} - Z^+_{j+\frac{1}{2},k} + w^-_{j+\frac{1}{2},k} - Z^-_{j+\frac{1}{2},k}\big)\big((h_1)^+_{j+\frac{1}{2},k} - (h_1)^-_{j+\frac{1}{2},k}\big)\\
&\qquad\qquad + \frac{g}{2}\big(Z^+_{j+\frac{1}{2},k} + Z^-_{j+\frac{1}{2},k}\big)\big(w^+_{j+\frac{1}{2},k} - w^-_{j+\frac{1}{2},k}\big)\Big],\\
&C^{(1)}_{\boldsymbol{\Psi},j,k+\frac{1}{2}} = C^{(2)}_{\boldsymbol{\Psi},j,k+\frac{1}{2}} = C^{(4)}_{\boldsymbol{\Psi},j,k+\frac{1}{2}} = C^{(5)}_{\boldsymbol{\Psi},j,k+\frac{1}{2}} = 0,\\
&C^{(3)}_{\boldsymbol{\Psi},j,k+\frac{1}{2}} = -\frac{g}{2}\big((h_1)^+_{j,k+\frac{1}{2}} + (h_1)^-_{j,k+\frac{1}{2}}\big)\big(w^+_{j,k+\frac{1}{2}} - w^-_{j,k+\frac{1}{2}}\big),\\
&C^{(6)}_{\boldsymbol{\Psi},j,k+\frac{1}{2}} = \Big[-\frac{gr}{2}\big(w^+_{j,k+\frac{1}{2}} - Z^+_{j,k+\frac{1}{2}} + w^-_{j,k+\frac{1}{2}} - Z^-_{j,k+\frac{1}{2}}\big)\big((h_1)^-_{j,k+\frac{1}{2}} - (h_1)^-_{j,k+\frac{1}{2}}\big)\\
&\qquad\qquad + \frac{g}{2}\big(Z^+_{j,k+\frac{1}{2}} + Z^-_{j,k+\frac{1}{2}}\big)\big(w^-_{j,k+\frac{1}{2}} - w^-_{j,k+\frac{1}{2}}\big)\Big].
\end{aligned}$$

Remark 6.3. As in the 1-D case, in all of the 2-D numerical examples presented in §7, we have implemented the WENO-Z interpolation procedure using the local characteristic decomposition, which is similar to the 1-D one described in Remark 6.2.

7. Numerical examples

In this section, we test the proposed fifth-order A-WENO PCCU schemes on several numerical examples and compare their performance with that of the corresponding second-order FV PCCU schemes. The tested schemes will be referred to as the 5-Order Scheme and 2-Order Scheme, respectively.

Without other specification, we use the CFL number 0.5 and the systems of ODEs obtained after the semi-discretization (4.1) and (5.2) are integrated in time using the three-stage third-order strong stability preserving (SSP) Runge-Kutta solver; see, e.g., [17,18]. The 2-Order Scheme has been implemented with the minmod parameter $\theta = 1$. In Example 1, we use the 2π-periodic boundary conditions and in the Examples 2–9, we use free boundary conditions.

7.1. 1-D two-layer shallow water equations

We begin with four 1-D examples. In Example 2–5, we take sufficiently large computational domains (in Examples 2 and 3 we make sure that no waves reach the boundaries until the final computational time).

Example 1 *(Smooth Initial Data).* In this example, we consider the system (6.1) with $g = 9.81$, $r = 0.98$, the flat bottom topography $Z(x) \equiv 0$, and following smooth initial data:

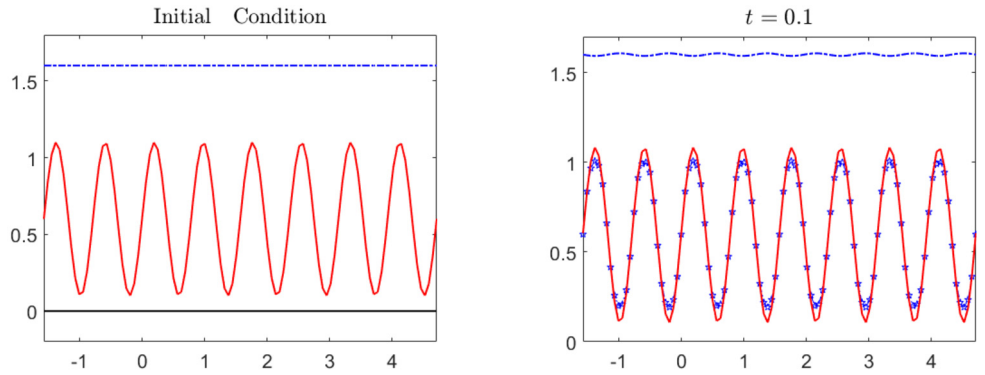

Fig. 7.1. Example 1: Initial water surface $h_1 + w$ and interface w (left) and the solutions ($h_1 + w$ and w) computed by the 5-Order and 2-Order Schemes at $t = 0.1$ (right). The dash-dotted blue line represents the water surface computed by the 5-Order Scheme, and the computed interfaces on the right are plotted using the solid red line (5-Order) and blue starts (2-Order). (For interpretation of the colors in the figure(s), the reader is referred to the web version of this article.)

Table 7.1
Example 1: L^1-errors and experimental convergence rates for $h_1 + w$ and h_1 for both the 5-Order and 2-Order Schemes.

Δx	5-Order Scheme				2-Order Scheme			
	$h_1 + w$		h_1		$h_1 + w$		h_1	
	Error	Rate	Error	Rate	Error	Rate	Error	Rate
$\pi/50$	1.79e-02	–	7.33e-02	–	9.11e-03	–	5.02e-01	–
$\pi/100$	8.62e-05	7.69	2.73e-03	4.74	1.39e-03	2.71	8.53e-02	2.56
$\pi/200$	7.34e-06	3.55	6.26e-05	5.44	1.89e-04	2.87	1.73e-02	2.30
$\pi/400$	2.29e-07	5.01	1.18e-06	5.72	2.97e-05	2.67	2.75e-03	2.66
$\pi/800$	5.55e-09	5.37	9.28e-09	6.99	3.66e-06	3.02	2.96e-04	3.22

$$\big(h_1(x,0), q_1(x,0), w(x,0), q_2(x,0)\big) = \Big(1 - \frac{1}{2}\sin(8x), 0, 0.6 + \frac{1}{2}\sin(8x), 0\Big).$$

We first compare the experimental rates of convergence of the studied 5-Order and 2-Order Schemes. To this end, we take the computational domain $[-\pi/2, 3\pi/2]$ and compute the numerical solutions until a small final time $t = 0.1$, by which the exact solution remains smooth. The initial state and the results obtained using a uniform mesh $\Delta x = \pi/50$ are shown in Fig. 7.1.

We then refine the mesh and compute the solutions on a sequence of uniform meshes with $\Delta x = \pi/25$, $\pi/50$, $\pi/100$, $\pi/200$, $\pi/400$ and $\pi/800$. In these computations, we use the CFL number $\frac{1}{10}(\Delta x)^{2/3}$ (instead of 0.5) as we use the third-order SSP Runge-Kutta ODE solver and we would like to balance the spatial and temporal errors for the 5-Order Scheme. We estimate the L^1-errors and the experimental convergence rates based on the consecutive grids using the following formulae:

$$\text{Error}(\Delta x) \approx ||(\cdot)^{\Delta x} - (\cdot)^{\Delta x/2}||_{L^1}, \quad \text{Rate}(\Delta x) = \frac{\text{Error}(\Delta x)}{\text{Error}(\Delta x/2)},$$

where $(\cdot)^{\Delta x}$ denotes a certain quantity computed using a uniform mesh with the cell size Δx. The obtained results for $h_1 + w$ and h_1 are reported in Table 7.1, where one can clearly see that the achieved convergence rates even exceed the formal orders for both schemes.

We also run the computations on a very fine mesh with $\Delta x = \pi/800$ until a much larger final time $t = 40$, by which the solution clearly develops discontinuities. We show the interface w computed by the 5-Order and 2-Order Schemes and see that the 5-Order Scheme clearly outperforms its second-order counterpart; see Fig. 7.2 (top row). To further verify the convergence, we perform another mesh refinement and obtain the corresponding 5-Order and 2-Order solutions using $\Delta x = \pi/1600$; see Fig. 7.2 (bottom row).

Example 2 *(Small Perturbation of a Stationary Steady-State Solution).* In this example, we demonstrate the ability of the developed 5-Order Scheme to accurately capture quasi-steady states. This example is taken from [26, §2.7.2]. The initial data contain a small perturbation of the "lake-at-rest" steady state and are given by

$$(h_1, q_1, w, q_2)(x,0) = \begin{cases} (1 + 10^{-5}, 0, -1, 0) & \text{if } 0.1 < x < 0.2, \\ (1, 0, -1, 0) & \text{otherwise.} \end{cases}$$

The constant gravitational acceleration is $g = 10$, the density ratio is $r = 0.98$, and the bottom topography is

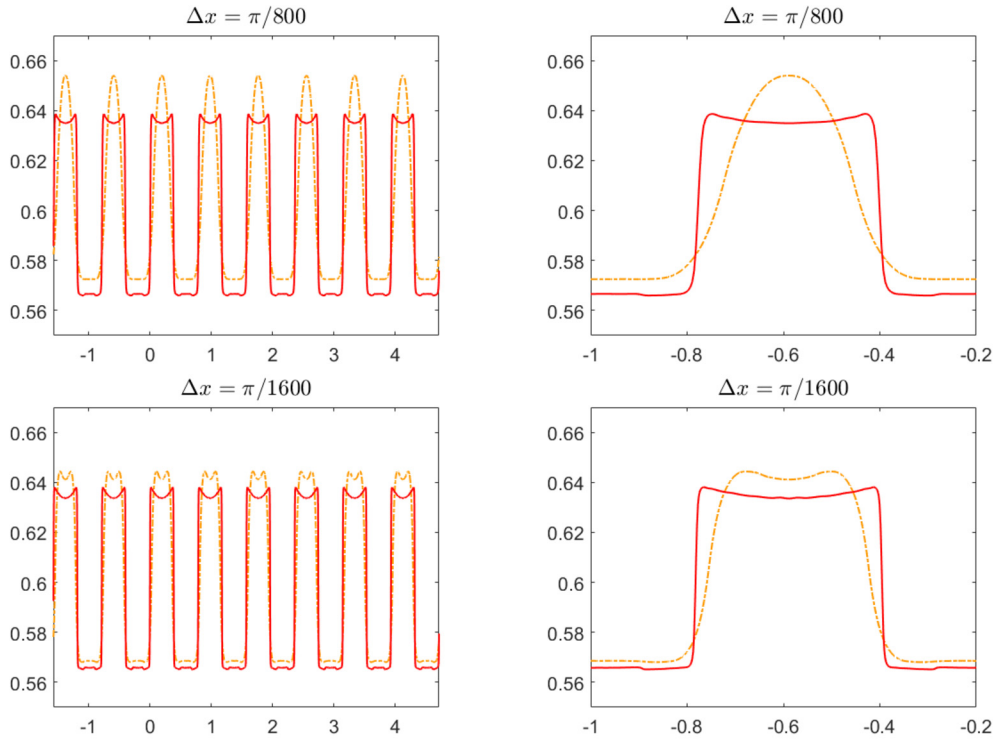

Fig. 7.2. Example 1: Interface w computed by the 5-Order (solid red line) and 2-Order (dash-dotted orange line) Schemes at $t = 40$ (left column) with the zoom at $[-1, 0.2]$ (right column). The results are obtained using $\Delta x = \pi/800$ (top row) and $\Delta x = \pi/1600$ (bottom row).

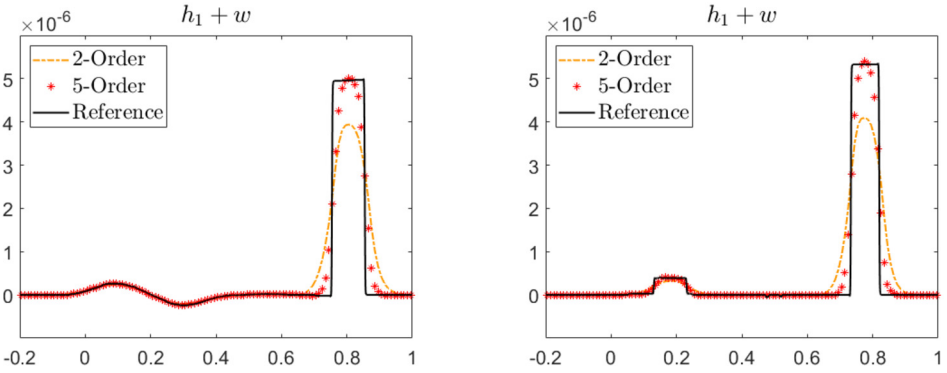

Fig. 7.3. Example 2: Water surface $h_1 + w$ computed by the 5-Order and 2-Order Schemes for the smooth (left) and nonsmooth (right) bottom topographies. The reference solutions are computed using the 5-Order Scheme on a fine mesh with $\Delta x = 1/1600$.

$$Z(x) = \begin{cases} 0.25\big[\cos(10\pi\,(x - 0.5)) + 1\big] - 2 & \text{if } 0.4 < x < 0.6, \\ -2 & \text{otherwise.} \end{cases} \tag{7.1}$$

We compute the numerical solution by the 5-Order and 2-Order Schemes on the computational domain $[-0.2, 1]$ using a uniform mesh with $\Delta x = 1/100$. In Fig. 7.3 (left), we present the fluctuation of the water surface $h_1 + w$ at time $t = 0.15$. As expected, no oscillations have been generated by both of the studied well-balanced schemes. At the same time, one can observe a much higher resolution achieved by the 5-Order Scheme.

We then replace the smooth bottom topography function (7.1) with the following discontinuous one:

$$Z(x) = \begin{cases} -1.5 & \text{if } x > 0.5, \\ -2 & \text{otherwise.} \end{cases}$$

The obtained results are reported in Fig. 7.3 (right), where one can see once again that the 5-Order Scheme clearly outperforms the 2-Order Scheme.

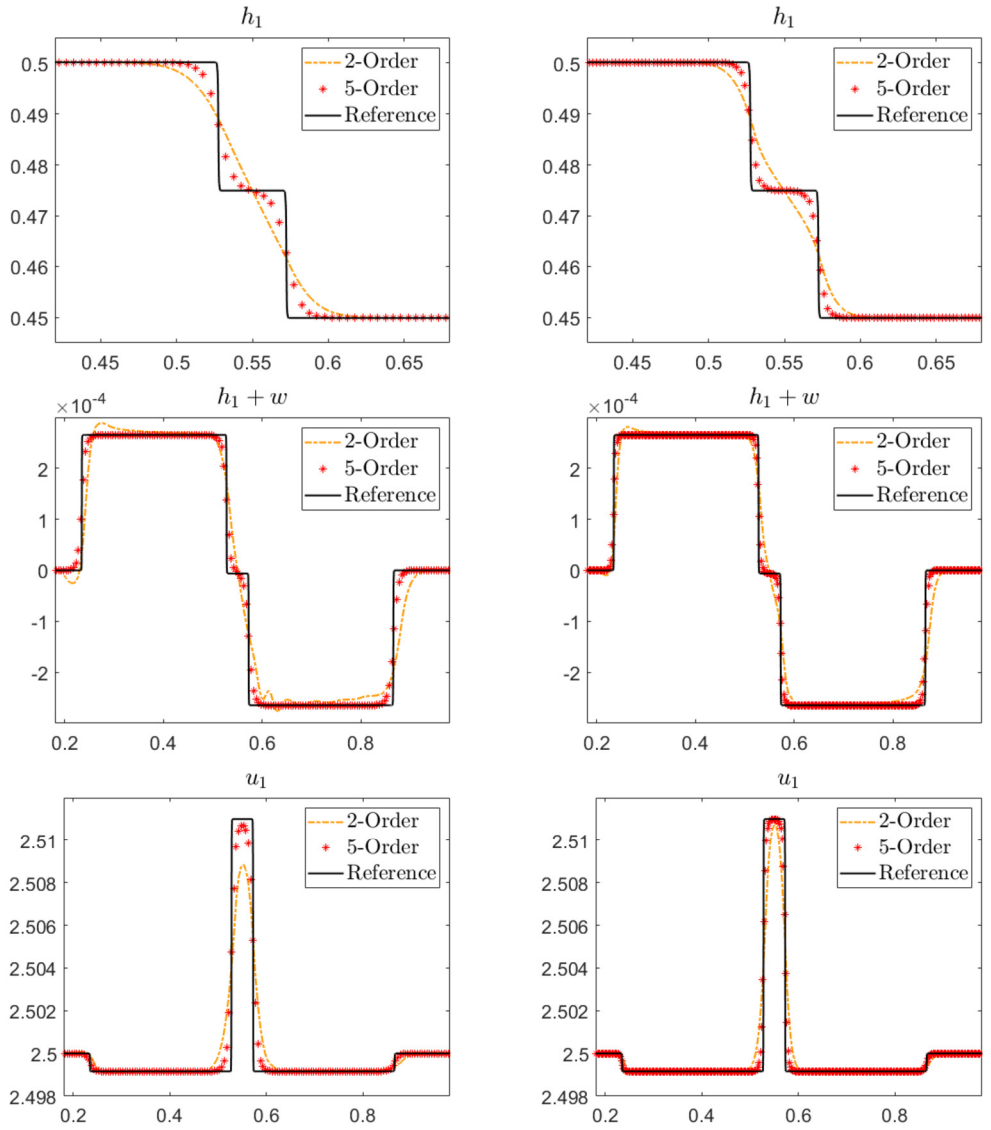

Fig. 7.4. Example 3, first test: Upper layer h_1 zoomed at the interface area (upper row), water surface $h_1 + w$ (middle row), and velocity of the upper layer u_1 (lower row) computed using $\Delta x = 1/200$ (left column) and $1/400$ (right column). The reference solution is computed by the 5-Order Scheme on a very fine mesh with $\Delta x = 1/10000$.

Example 3 *(Interface Propagation).* In this example, we numerically study the propagation of the interface and compare the numerical results of the 5-Order and 2-Order Schemes. We consider two test problems taken from [26, §2.7.3]. In the first test, we capture the propagation of the interface, initially located at $x = 0.3$:

$$(h_1, q_1, w, q_2)(x, 0) = \begin{cases} (0.50, 1.250, -0.50, 1.250) & \text{if } x < 0.3, \\ (0.45, 1.125, -0.45, 1.375) & \text{otherwise.} \end{cases}$$

The bottom topography is flat ($Z(x) \equiv -1$), the constant gravitational acceleration is $g = 10$, and the density ratio is $r = 0.98$. The exact solution of the studied Riemann problem is unavailable. However, a reference solution presented in [26, Figure 2.4] clearly indicates that the interface between the layers (h_1) contains an intermediate flat state at the level $h_1 \approx 0.475$. One can also see in [26, Figure 2.4] that the second-order CU scheme from [26] requires a relatively fine mesh to capture this intermediate state. We compute the numerical solutions by the 5-Order and 2-Order Schemes at time $t = 0.1$ using two uniform meshes with $\Delta x = 1/200$ and $1/400$ on the computational domain $[-1, 1]$. The obtained results are shown in Figs. 7.4. As one can clearly see, the intermediate flat state is much better resolved by the 5-Order Scheme. This can be observed in both interface (h_1) and water surface ($h_1 + w$) plots. In the region of that intermediate state, the velocity u_1 develops a flat plateau, which is also substantially better resolved by the 5-Order Scheme. This clearly indicates that the

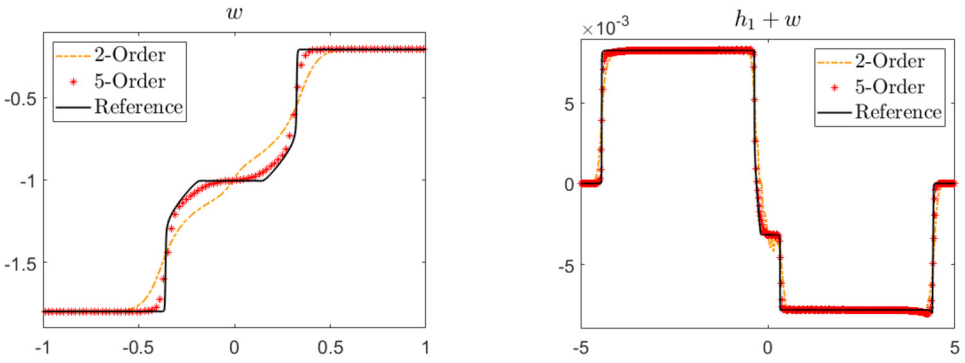

Fig. 7.5. Example 3, second test: w-component of the solution zoomed at the interface area (left) and water surface $h_1 + w$ (right). The reference solution is computed using the 5-Order Scheme on a very fine mesh with $\Delta x = 1/500$.

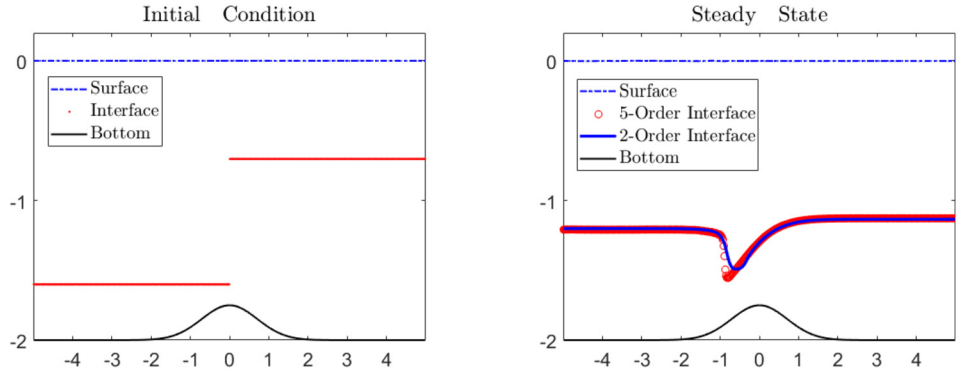

Fig. 7.6. Example 4: Water surface $h_1 + w$, interface w and bottom topography Z for the initial data (left) and the corresponding discrete steady states (right).

5-Order Scheme outperforms the 2-Order Scheme and justifies the use of the higher-order scheme even in examples with Riemann initial data, for which smooth parts of the solution are typically very simple (piecewise constant in this particular example).

Next, we consider the second test with a much larger initial jump at the interface:

$$(h_1, q_1, w, q_2)(x, 0) = \begin{cases} (1.8, 0, -1.8, 0) & \text{if } x < 0, \\ (0.2, 0, -0.2, 0) & \text{otherwise.} \end{cases}$$

The bottom topography is again flat ($Z(x) \equiv -2$), the constant gravitational acceleration is $g = 9.81$, and the density ratio is $r = 0.98$. The solutions computed by the 5-Order and 2-Order Schemes at time $t = 1$ using a uniform grid with $\Delta x = 1/50$ on the computational domain $[-5, 5]$ are presented in Fig. 7.5. Even though the structure of the intermediate state is now more complicated than in the first interface propagation test, the 5-Order Scheme still achieves a much higher resolution and clearly outperforms the 2-Order Scheme.

Example 4 *(Internal Dam Break).* In this example, we test the ability of the proposed 5-Order Scheme to accurately capture discontinuous steady-state solutions. To this end, we model an internal dam break over a nonflat bottom using the following initial data:

$$(h_1, q_1, w, q_2)(x, 0) = \begin{cases} (1.6, 0, -1.6, 0) & \text{if } x < 0, \\ (0.7, 0, -0.7, 0) & \text{otherwise,} \end{cases}$$

and the continuous bottom topography

$$Z(x) = 0.25e^{-x^2} - 2.$$

The constant gravitational acceleration is $g = 9.81$ and the density ratio is $r = 0.998$. We take the computational domain $[-5, 5]$, which is sufficiently large to eliminate any significant influence of the boundary conditions on the computed solutions. The initial setting is shown in Fig. 7.6 (left). The solution of the studied initial-boundary value problem is expected to converge to a steady state containing a hydraulic jump, which makes this test problem quite challenging.

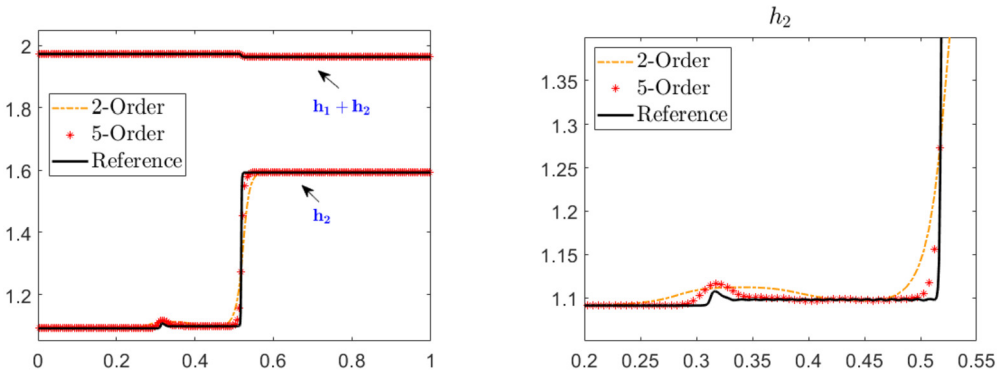

Fig. 7.7. Example 5: Lower layer h_2 and water depth $h_1 + h_2$ (left) and lower layer h_2 zoomed at $[0.2, 0.55]$ (right). The reference solution is computed using the 5-Order Scheme on a very fine mesh with $\Delta x = 1/1000$.

We compute the numerical solutions by both the 5-Order and 2-Order Schemes using a uniform grid with $\Delta x = 1/50$ on the computational domain $[-5, 5]$ until they converge to their corresponding discrete steady states. The obtained results are shown in Fig. 7.6 (right), where one can observe that the 5-Order Scheme sharply resolves the discontinuous interface, which is significantly smeared by the 2-Order Scheme.

Example 5 *(Riemann Problem).* In this example taken from [7, §4.2], the initial data are

$$(h_1, q_1, w, q_2)(x, 0) = \begin{cases} (0.8817, -0.1738, 1.589125, 0.1613) & \text{if } x < 0.5, \\ (0.37, -0.1868, 2.578625, 0.1742) & \text{otherwise,} \end{cases}$$

and the bottom topography $Z(x) \equiv 0.983925$ is flat. The constant gravitational acceleration is $g = 9.81$ and the density ratio is $r = 0.98$. We compute the numerical solutions on the computational domain $[0, 1]$ by both the 5-Order and 2-Order Schemes using a uniform mesh with $\Delta x = 1/200$ until the final time $t = 0.6$. The obtained results are shown in Figs. 7.7. As one can clearly see, the 5-Order Scheme achieves a substantially higher resolution of the internal wave than the 2-Order Scheme.

7.2. 2-D two-layer shallow water equations

Example 6 *(Interface Propagation).* This example, taken from [26, §3.71], is a 2-D extension of the 1-D Example 3: a round-shape interface propagates in the northeast direction, that is, to the right and upward. The initial data are

$$(h_1, q_1, p_1, w, q_2, p_2)(x, y, 0) = \begin{cases} (0.50, 1.250, 1.250, -0.50, 1.250.1.250) & \text{if } (x, y) \in \Omega, \\ (0.45, 1.125, 1.125, -0.45, 1.375, 1.375) & \text{otherwise,} \end{cases}$$

where $\Omega = \{x < -0.5, y < 0\} \cup \{(x + 0.5)^2 + (y + 0.5)^2 < 0.25\} \cup \{x < 0, y < -0.5\}$. The constant gravitational acceleration is $g = 10$ and the density ratio is $r = 0.98$. The bottom topography in this example is flat ($Z(x, y) \equiv -1$).

We compute the numerical solutions by both the 5-Order and 2-Order Schemes until the final time $t = 0.1$ on the computational domain $[-0.55, 0.7] \times [-0.55, 0.7]$ on a sequence of uniform meshes with $\Delta x = \Delta y = 1/200$, $1/400$ and $1/800$. The results obtained by the 5-Order Scheme are shown in Fig. 7.8. As one can see, the structure of this 2-D solution is similar to the 1-D solution in Example 3 and it also matches pretty well the results reported in [26, Figure 3.1]. As in the 1-D case, an intermediate state emerges. This can be observed in Fig. 7.9, where we plot the diagonal slices of the upper layer h_1 computed by both the 5-Order and 2-Order Schemes. One can also clearly see that the 5-Order Scheme resolves the intermediate state much better than the 2-Order Scheme. This improvement in the 2-D result is especially important since the 2-D mesh refinement is very computationally expensive.

In order to check the efficiency of the proposed 5-Order Scheme, we perform a more thorough comparison between the 5-Order and 2-Order Schemes by taking into account an additional computational cost of the 5-Order Scheme. To this end, we first measure the CPU time consumed by the 5-Order Scheme on a uniform mesh with $\Delta x = \Delta y = 1/200$ and then refine the mesh in the 2-Order computations to the level $\Delta x = \Delta y = 1/450$, for which approximately the same CPU time is consumed by the 2-Order Scheme to compute the numerical solutions at the final time $t = 0.1$. Diagonal slices of the upper layer h_1 computed by the 5-Order and 2-Order Schemes are plotted in Fig. 7.10. As one can clearly see, the 5-Order Scheme achieves a better resolution despite using substantially coarser mesh.

Example 7 *(Interface Propagation over a Nonflat Bottom).* We now follow [26, §3.7.2] and extend the previous example to the case of a nonflat bottom topography. We take the Gaussian-shaped bottom function

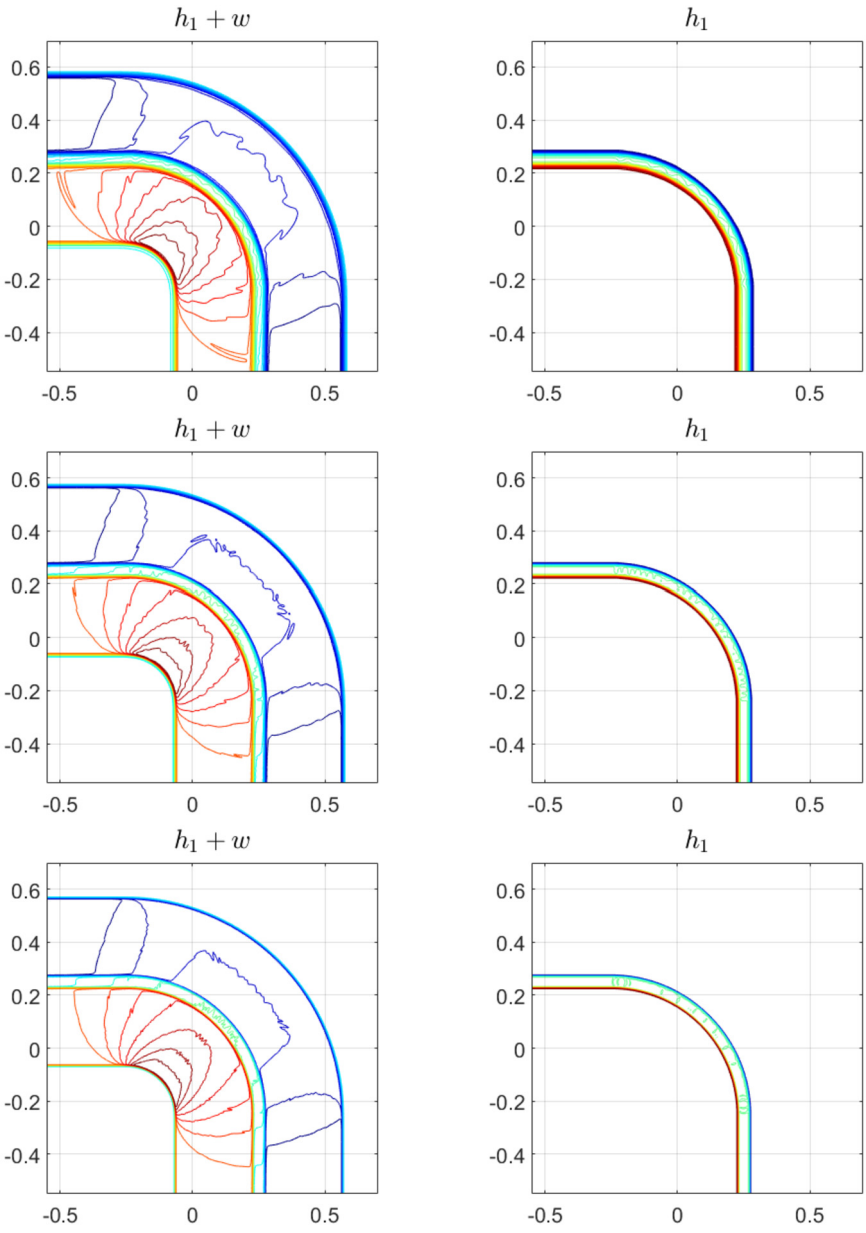

Fig. 7.8. Example 6: Water surface $h_1 + w$ and the upper layer h_1 computed on three uniform grids with $\Delta x = \Delta y = 1/200$ (upper row), $1/400$ (middle row) and $1/800$ (lower row).

$$Z(x, y) = 0.05e^{-100(x^2+y^2)} - 1,$$

and the following initial data:

$$(h_1, q_1, p_1, w, q_2, p_2)(x, y, 0) = \begin{cases} (0.50, 2.5, 2.5, -0.50, 2.5, 2.5) & \text{if } (x, y) \in \Omega, \\ (0.45, 2.5, 2.5, -0.45, 2.5, 2.5) & \text{otherwise,} \end{cases}$$

where Ω is as defined in Example 6. The constant gravitational acceleration is $g = 10$ and the density ratio is $r = 0.98$.

We compute the numerical solution until the final time $t = 0.1$ by the 5-Order Scheme on the computational domain $[-0.55, 0.7] \times [-0.55, 0.7]$ on a sequence of uniform meshes with $\Delta x = \Delta y = 1/200$, $1/400$, and $1/800$. The results are shown in Fig. 7.11. Due to a nonflat bottom topography, the solution of this problem develops a very complicated wave structure. The obtained numerical solution seems to be convergent. Compared to the results reported in [26, Figure 3.3], one can observe not only a sharper resolution of the intermediate state, but also substantially less oscillatory behavior of

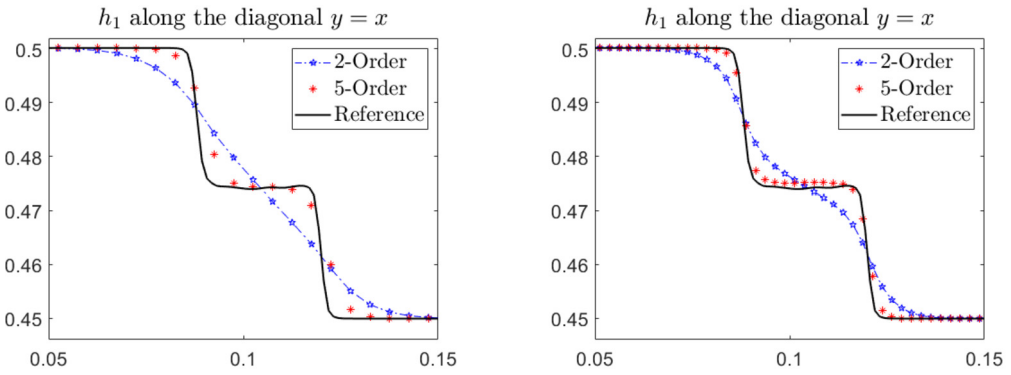

Fig. 7.9. Example 6: Diagonal slices of the upper layer h_1 computed by the 5-Order and 2-Order Schemes with $\Delta x = \Delta y = 1/200$ (left) and $1/400$ (right). Zoom at the interface area. The reference solution is calculated by the 5-Order Scheme with $\Delta x = \Delta y = 1/800$.

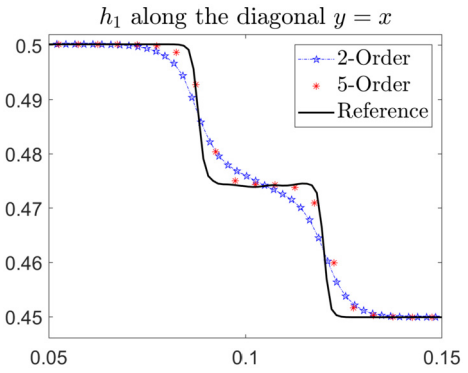

Fig. 7.10. Example 6: Diagonal slices of the upper layer h_1 computed by the 5-Order Scheme with $\Delta x = \Delta y = 1/200$ and the 2-Order Scheme with $\Delta x = \Delta y = 1/450$. Zoom at the interface area. The reference solution is calculated by the 5-Order Scheme with $\Delta x = \Delta y = 1/800$.

our solution. The latter can be attributed to the local characteristic decomposition implemented in the proposed 5-Order Scheme.

Example 8 *(Internal Circular Dam Break over Flat Bottom Topography).* In this example taken from [6, §7.4.1], we consider an internal circular dam-break problem with flat bottom topography. The initial conditions are given by

$$(h_1, q_1, p_1, w, q_2, p_2)(x, y, 0) = \begin{cases} (1.8, 0, 0, -1.8, 0, 0) & \text{if } x^2 + y^2 > 4, \\ (0.2, 0, 0, -0.2, 0, 0) & \text{otherwise.} \end{cases}$$

The constant gravitational acceleration is $g = 9.81$, the density ratio is $r = 0.998$, and the flat bottom topography is $Z(x, y) \equiv -2$.

We compute the numerical solutions on the domain $[-5, 5] \times [-5, 5]$ using both the 5-Order and 2-Order Schemes at times $t = 4$, 6, 10, 14, 16, and 20 on a uniform mesh with $\Delta x = \Delta y = 1/20$. In Fig. 7.12, we present the slices of the interface w, the surface $h_1 + w$ and the bottom topography Z along the diagonal $y = x$ for different computational times. As one can see, the 5-Order Scheme leads to significantly better resolution than the 2-Order Scheme.

Example 9 *(Internal Circular Dam Break over Nonflat Bottom Topography).* In the last example taken from [12, §5.11], we consider an internal circular dam-break problem with nonflat bottom topography. The initial conditions are given by

$$(h_1, q_1, p_1, w, q_2, p_2)(x, y, 0) = \begin{cases} (1.8, 0, 0, -1.8, 0, 0) & \text{if } x^2 + y^2 > 1, \\ (0.2, 0, 0, -0.2, 0, 0) & \text{otherwise,} \end{cases}$$

the constant gravitational acceleration is $g = 9.81$, the density ratio is $r = 0.98$, and the nonflat bottom topography is $Z(x, y) \equiv -2 + 0.5e^{(x^2+y^2)}$.

We compute the numerical solutions on the domain $[-2, 2] \times [-2, 2]$ using a uniform mesh with $\Delta x = \Delta y = 1/50$ by both the 5-Order and 2-Order Schemes at times $t = 1$ and 2. In Fig. 7.13, we present the interface w computed by the 5-Order and 2-Order Schemes and in Fig. 7.14, we present the slices along $y = 0$ of the interface w computed at different

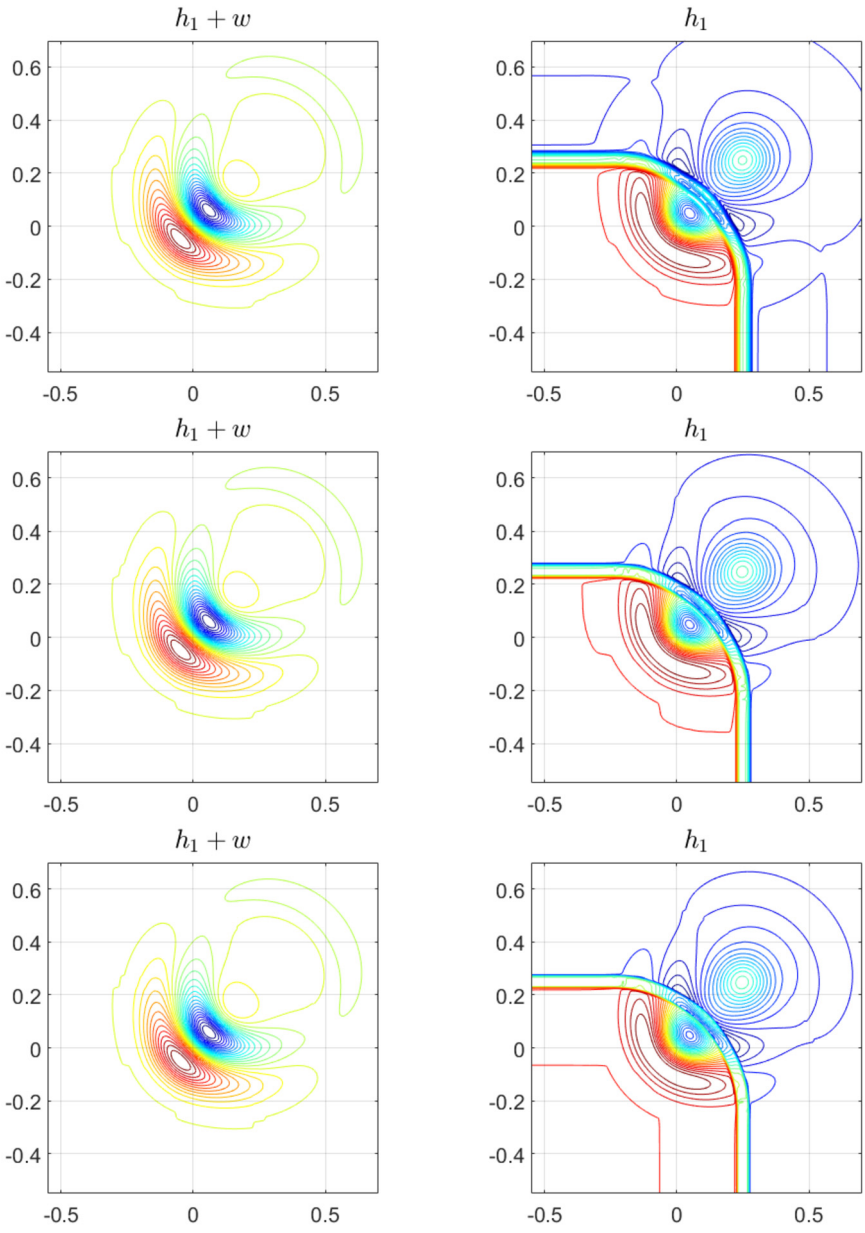

Fig. 7.11. Example 7: Water surface $h_1 + w$ and the upper layer h_1 computed on three uniform grids with $\Delta x = \Delta y = 1/200$ (upper row), $1/400$ (middle row) and $1/800$ (lower row).

times. One can observe that despite developing small water surface oscillations, the 5-Order Scheme achieves much higher resolution than the 2-Order Scheme.

8. Conclusion

In this paper, we have extended the second-order finite-volume path-conservative central-upwind (PCCU) schemes to the fifth-order of accuracy in the framework of finite-difference A-WENO schemes. The developed fifth-order A-WENO PCCU schemes have been applied to particular nonconservative systems—the 1-D and 2-D two-layer shallow water equations. We have shown that the proposed schemes are well-balanced in the sense that they are capable of exactly preserving "lake-at-rest" steady states. We have tested the new fifth-order schemes on a number of numerical examples and demonstrated that they outperform their second-order counterparts despite an increased computational cost per time step (the computational cost has been taken into account to illustrate higher efficiency of the fifth-order PCCU schemes).

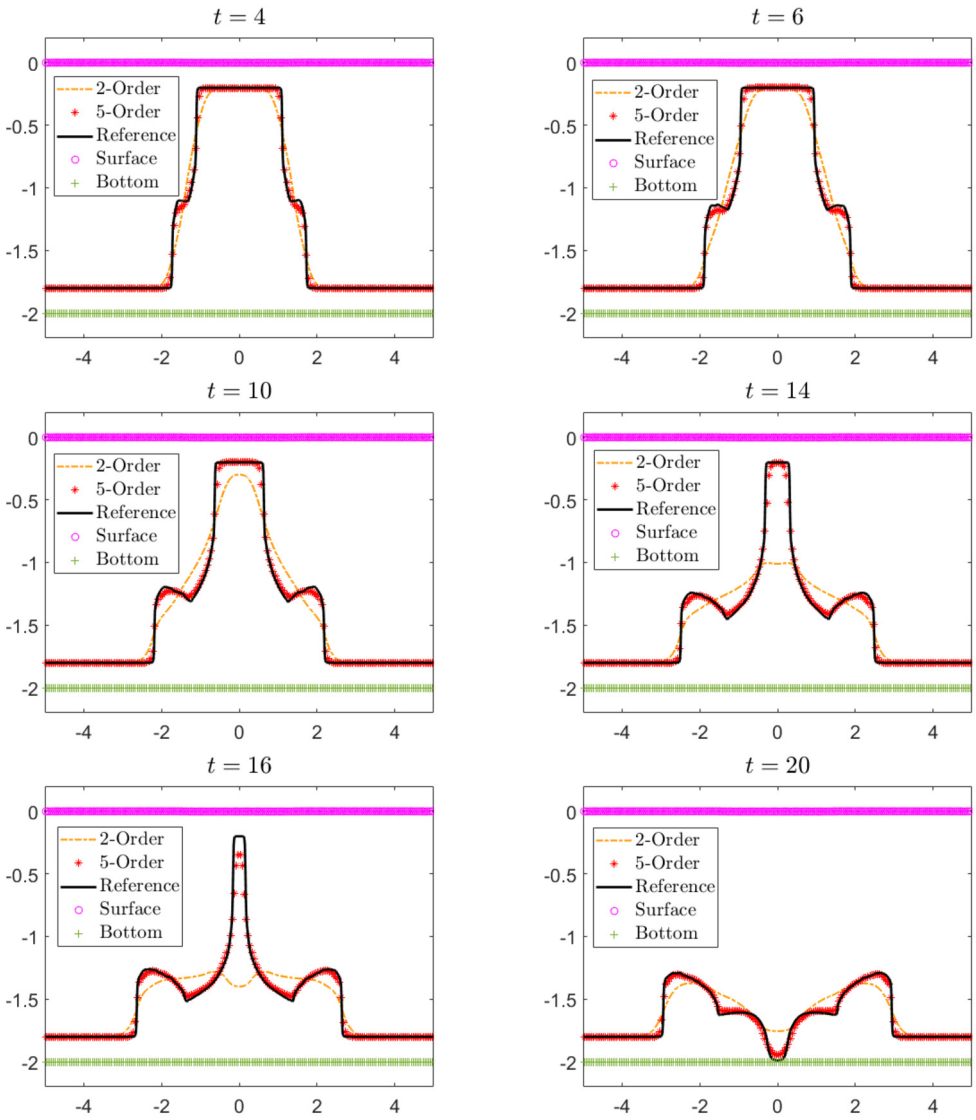

Fig. 7.12. Example 8: Diagonal slices of the interface w, the water surface $h_1 + w$ and the bottom topography Z computed by the 5-Order and 2-Order Schemes with $\Delta x = \Delta y = 1/20$ at different times. The reference solution is calculated by the 5-Order Scheme with $\Delta x = \Delta y = 1/80$.

The proposed A-WENO approach can be extended to the case of more general steady states via the flux globalization technique. This extension will be studied in our future work.

Funding

The work of A. Kurganov was supported in part by NSFC grants 11771201, 12171226, and 12111530004, and by the fund of the Guangdong Provincial Key Laboratory Of Computational Science And Material Design (No. 2019B030301001).

CRediT authorship contribution statement

Shaoshuai Chu: Conceptualization, Investigation, Methodology, Software, Validation, Visualization, Writing – original draft, Writing – review & editing. **Alexander Kurganov:** Conceptualization, Funding acquisition, Investigation, Methodology, Project administration, Software, Supervision, Validation, Writing – original draft, Writing – review & editing. **Mingye Na:** Conceptualization, Investigation, Methodology, Software, Validation, Visualization, Writing – original draft, Writing – review & editing.

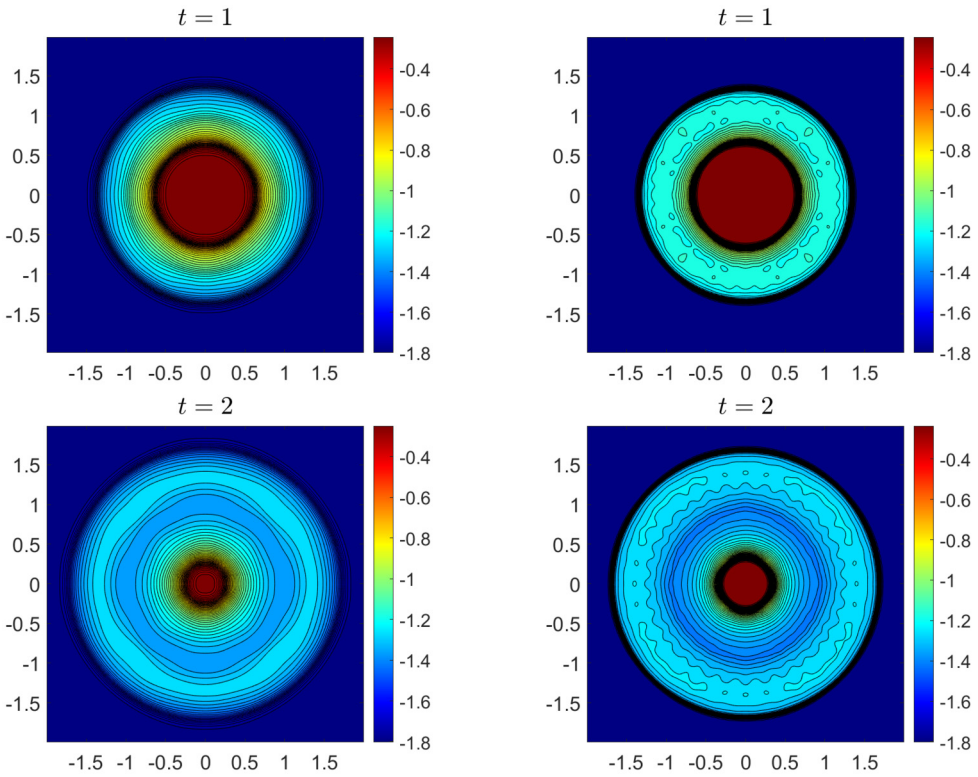

Fig. 7.13. Example 9: Water interface w computed by the 2-Order (left) and 5-Order (right) Schemes at different times.

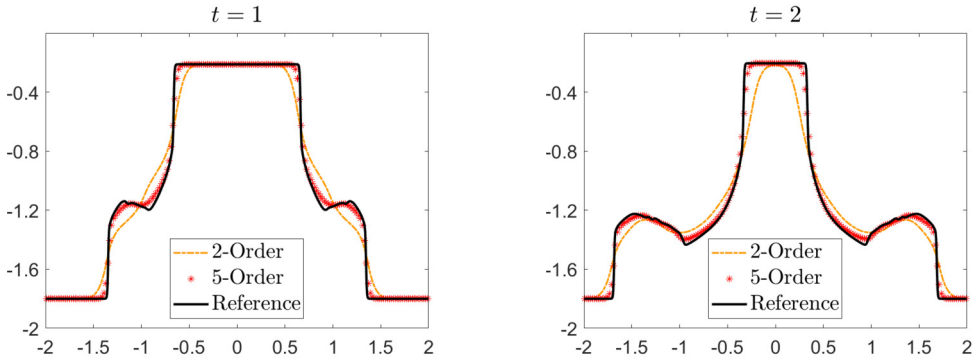

Fig. 7.14. Example 9: Longitudinal slices along $y = 0$ of the interface w computed by the 5-Order and 2-Order Schemes with $\Delta x = \Delta y = 1/50$ at $t = 1$ and 2. The reference solution is calculated by the 5-Order Scheme with $\Delta x = \Delta y = 1/200$.

Data and software availability

The data that support the findings of this study and FORTRAN codes developed by the authors and used to obtain all of the presented numerical results are available from the corresponding author upon reasonable request.

Declaration of competing interest

On behalf of all authors, the corresponding author states that there is no conflict of interest.

References

[1] R. Abgrall, S. Karni, Two-layer shallow water system: a relaxation approach, SIAM J. Sci. Comput. 31 (2009) 1603–1627.
[2] C. Berthon, F. Foucher, T. Morales, An efficient splitting technique for two-layer shallow-water model, Numer. Methods Partial Differ. Equ. 31 (2015) 1396–1423.

[3] F. Bouchut, Nonlinear Stability of Finite Volume Methods for Hyperbolic Conservation Laws and Well-Balanced Schemes for Sources, Frontiers in Mathematics, Birkhäuser Verlag, Basel, 2004.
[4] F. Bouchut, T. Morales de Luna, An entropy satisfying scheme for two-layer shallow water equations with uncoupled treatment, ESAIM Math. Model. Numer. Anal. 42 (2008) 683–698.
[5] S. Busto, M. Dumbser, S. Gavrilyuk, K. Ivanova, On thermodynamically compatible finite volume methods and path-conservative ADER discontinuous Galerkin schemes for turbulent shallow water flows, J. Sci. Comput. 88 (2021) 28.
[6] M.J. Castro, E.D. Fernández-Nieto, A.M. Ferreiro, J.A. García-Rodríguez, C. Parés, High order extensions of Roe schemes for two-dimensional nonconservative hyperbolic systems, J. Sci. Comput. 39 (2009) 67–114.
[7] M.J. Castro, U.S. Fjordholm, S. Mishra, C. Parés, Entropy conservative and entropy stable schemes for nonconservative hyperbolic systems, SIAM J. Numer. Anal. 51 (2013) 1371–1391.
[8] M.J. Castro, A. Kurganov, T. Morales de Luna, Path-conservative central-upwind schemes for nonconservative hyperbolic systems, ESAIM Math. Model. Numer. Anal 53 (2019) 959–985.
[9] M.J. Castro, J. Macías, C. Parés, A Q-scheme for a class of systems of coupled conservation laws with source term. Application to a two-layer 1-D shallow water system, ESAIM Math. Model. Numer. Anal. 35 (2001) 107–127.
[10] M.J. Castro, T. Morales de Luna, C. Parés, Well-balanced schemes and path-conservative numerical methods, in: Handbook of Numerical Methods for Hyperbolic Problems, in: Handb. Numer. Anal., vol. 18, Elsevier/North-Holland, Amsterdam, 2017, pp. 131–175.
[11] M.J. Castro, C. Parés, Well-balanced high-order finite volume methods for systems of balance laws, J. Sci. Comput. 82 (2020) 48.
[12] M.J. Castro, C. Parés, G. Puppo, G. Russo, Central schemes for nonconservative hyperbolic systems, SIAM J. Sci. Comput. 34 (2012) B523–B558.
[13] M.J. Castro-Díaz, E.D. Fernández-Nieto, J.M. González-Vida, C. Parés-Madronal, Numerical treatment of the loss of hyperbolicity of the two-layer shallow-water system, J. Sci. Comput. 48 (2011) 16–40.
[14] C. Chalons, Path-conservative in-cell discontinuous reconstruction schemes for non conservative hyperbolic systems, Commun. Math. Sci. 18 (2020) 1–30.
[15] G. Dal Maso, P.G. Lefloch, F. Murat, Definition and weak stability of nonconservative products, J. Math. Pures Appl. 74 (1995) 483–548.
[16] W.S. Don, D.-M. Li, Z. Gao, B.-S. Wang, A characteristic-wise alternative WENO-Z finite difference scheme for solving the compressible multicomponent non-reactive flows in the overestimated quasi-conservative form, J. Sci. Comput. 82 (2020) 27.
[17] S. Gottlieb, D. Ketcheson, C.-W. Shu, Strong Stability Preserving Runge-Kutta and Multistep Time Discretizations, World Scientific Publishing Co. Pte. Ltd., Hackensack, NJ, 2011.
[18] S. Gottlieb, C.-W. Shu, E. Tadmor, Strong stability-preserving high-order time discretization methods, SIAM Rev. 43 (2001) 89–112.
[19] G.S. Jiang, C.-W. Shu, Efficient implementation of weighted ENO schemes, J. Comput. Phys. 126 (1996) 202–228.
[20] Y. Jiang, C.-W. Shu, M.P. Zhang, An alternative formulation of finite difference weighted ENO schemes with Lax-Wendroff time discretization for conservation laws, SIAM J. Sci. Comput. 35 (2013) A1137–A1160.
[21] R. Klein, Scale-dependent models for atmospheric flows, Annu. Rev. Fluid Mech. 42 (1997) 249–272.
[22] A. Kurganov, Finite-volume schemes for shallow-water equations, Acta Numer. 27 (2018) 289–351.
[23] A. Kurganov, D. Levy, Central-upwind schemes for the Saint-Venant system, ESAIM Math. Model. Numer. Anal. 36 (2002) 397–425.
[24] A. Kurganov, C.-T. Lin, On the reduction of numerical dissipation in central-upwind schemes, Commun. Comput. Phys. 2 (2007) 141–163.
[25] A. Kurganov, S. Noelle, G. Petrova, Semidiscrete central-upwind schemes for hyperbolic conservation laws and Hamilton-Jacobi equations, SIAM J. Sci. Comput. 23 (2001) 707–740.
[26] A. Kurganov, G. Petrova, Central-upwind schemes for two-layer shallow water equations, SIAM J. Sci. Comput. 31 (2009) 1742–1773.
[27] A. Kurganov, M. Prugger, T. Wu, Second-order fully discrete central-upwind scheme for two-dimensional hyperbolic systems of conservation laws, SIAM J. Sci. Comput. 39 (2017) A947–A965.
[28] A. Kurganov, E. Tadmor, New high-resolution semi-discrete central schemes for Hamilton-Jacobi equations, J. Comput. Phys. 160 (2000) 720–742.
[29] P.G. LeFloch, Hyperbolic systems of conservation laws, in: The Theory of Classical and Nonclassical Shock Waves, in: Lectures in Mathematics ETH Zürich, Birkhäuser Verlag, Basel, 2002.
[30] P.G. Lefloch, Graph solutions of nonlinear hyperbolic systems, J. Hyperbolic Differ. Equ. 1 (2004) 643–689.
[31] K.-A. Lie, S. Noelle, On the artificial compression method for second-order nonoscillatory central difference schemes for systems of conservation laws, SIAM J. Sci. Comput. 24 (2003) 1157–1174.
[32] H. Liu, A numerical study of the performance of alternative weighted ENO methods based on various numerical fluxes for conservation law, Appl. Math. Comput. 296 (2017) 182–197.
[33] H. Liu, J. Qiu, Finite difference Hermite WENO schemes for conservation laws, II: an alternative approach, J. Sci. Comput. 66 (2016) 598–624.
[34] X. Liu, J. He, A well-balanced numerical model for depth-averaged two-layer shallow water flows, Comput. Appl. Math. 40 (2021) 311.
[35] H. Nessyahu, E. Tadmor, Nonoscillatory central differencing for hyperbolic conservation laws, J. Comput. Phys. 87 (1990) 408–463.
[36] T. Nonomura, K. Fujii, Characteristic finite-difference WENO scheme for multicomponent compressible fluid analysis: overestimated quasi-conservative formulation maintaining equilibriums of velocity, pressure, and temperature, J. Comput. Phys. 340 (2017) 358–388.
[37] C. Parés, Path-Conservative Numerical Methods for Nonconservative Hyperbolic Systems, Quad. Mat., Dept. Math., vol. 24, Seconda Univ. Napoli, Caserta, 2009.
[38] J. Pedlosky, Geophysical Fluid Dynamics, 2nd ed., Springer-Verlag, New York, 1987.
[39] E. Pimentel-García, M.J. Castro, C. Chalons, T. Morales de Luna, C. Parés, In-cell discontinuous reconstruction path-conservative methods for non conservative hyperbolic systems—second-order extension, J. Comput. Phys. 459 (2022) 111152.
[40] J. Qiu, C.-W. Shu, On the construction, comparison, and local characteristic decomposition for high-order central WENO schemes, J. Comput. Phys. 183 (2002) 187–209.
[41] K.A. Schneider, J.M. Gallardo, D.S. Balsara, B. Nkonga, C. Parés, Multidimensional approximate Riemann solvers for hyperbolic nonconservative systems. Applications to shallow water systems, J. Comput. Phys. 444 (2021) 110547.
[42] C.-W. Shu, High order weighted essentially nonoscillatory schemes for convection dominated problems, SIAM Rev. 51 (2009) 82–126.
[43] C.-W. Shu, Essentially non-oscillatory and weighted essentially non-oscillatory schemes, Acta Numer. 29 (2020) 701–762.
[44] P.K. Sweby, High resolution schemes using flux limiters for hyperbolic conservation laws, SIAM J. Numer. Anal. 21 (1984) 995–1011.
[45] G.K. Vallis, Atmospheric and Oceanic Fluid Dynamics: Fundamentals and Large-Scale Circulation, Cambridge University Press, 2006.
[46] B.-S. Wang, W.S. Don, N.K. Garg, A. Kurganov, Fifth-order A-WENO finite-difference schemes based on a new adaptive diffusion central numerical flux, SIAM J. Sci. Comput. 42 (2020) A3932–A3956.
[47] B.-S. Wang, W.S. Don, A. Kurganov, Y. Liu, Fifth-order A-WENO schemes based on the adaptive diffusion central-upwind Rankine-Hugoniot fluxes, Commun. Appl. Math. Comput. (2021), https://doi.org/10.1007/s42967-021-00161-2.
[48] B.-S. Wang, P. Li, Z. Gao, W.S. Don, An improved fifth order alternative WENO-Z finite difference scheme for hyperbolic conservation laws, J. Comput. Phys. 374 (2018) 469–477.
[49] V. Zeitlin, Geophysical Fluid Dynamics: Understanding (Almost) Everything with Rotating Shallow Water Models, Oxford University Press, Oxford, 2018.